# V446 Cephei: a $\beta$ Cep pulsator in a multiple system

A. Moharana,[1]★ J. Southworth,[1] K. Pavlovski,[2] A. Miszuda,[3] R. S. Rathour,[3,8] K. G. Hełminiak,[4] F. Marcadon,[3] D. M. Bowman,[5,6] T. B. Pawar,[7] and A. Tkachenko[6]

[1]*Astrophysics group, Keele University, ST5 5BG, Staffordshire, UK*
[2]*Department of Physics, Faculty of Science, University of Zagreb, 10 000 Zagreb, Croatia*
[3]*Nicolaus Copernicus Astronomical Center, Polish Academy of Sciences, ul. Bartycka 18, 00-716 Warszawa, Poland*
[4]*Nicolaus Copernicus Astronomical Center, Polish Academy of Sciences, ul. Rabiańska 8, 87-100 Toruń, Poland*
[5]*School of Mathematics, Statistics and Physics, Newcastle University, Newcastle upon Tyne NE1 7RU, UK*
[6]*Institute of Astronomy, KU Leuven, Celestijnenlaan 200D, 3001 Leuven, Belgium*
[7]*Villanova University, Dept. of Astrophysics and Planetary Sciences, 800 East Lancaster Avenue, Villanova, PA 19085, USA*
[8]*Université Côte d'Azur, Observatoire de la Côte d'Azur, CNRS, Laboratoire Lagrange, France*

Accepted XXX. Received YYY; in original form ZZZ

**ABSTRACT**

$\beta$ Cep stars in eclipsing binary (EB) systems give us an opportunity to put observational constraints on their structure and stellar parameters. We present a comprehensive analysis of the $\beta$ Cep star in the EB V446 Cep using *TESS* photometry and HERMES spectra. We calculate the stellar and orbital parameters using light curve modelling and spectral disentangling. The EB has an orbital period of 3.808567 ± 0.000012 d and a mass ratio of 0.1550 ± 0.0012. We derive the $\beta$ Cep star to have a mass of 10.68 ± 0.06 $M_\odot$, a radius of 5.864 ± 0.033 $R_\odot$, and $T_{\rm eff}$ = 24220 ± 180 K. We also extract the abundances of C, N, O, Mg, and Si for the $\beta$ Cep star, which are found to be consistent with galactic OB binaries. We identified 21 distinct pulsation frequencies, with the dominant mode at 10.24324 $d^{-1}$, which corresponds to a near-harmonic of the system's orbital frequency. The two stars in the EB have asynchronous rotation, with both stars rotating faster than the orbital frequency. We detect a companion to the EB using eclipse timing variations and period changes of the dominant pulsation frequency. We calculate the minimum mass of this tertiary companion to be 4.23 ± 0.46 $M_\odot$. Using spectral energy distributions and MIST isochrones, we conclude that V446 Cep is a co-evolving hierarchical quadruple with a close binary orbiting the EB on an orbit of 2408 d.

**Key words:** asteroseismology – binaries: eclipsing – stars: fundamental parameters – stars: massive – stars: individual: V446 Cep

## 1 INTRODUCTION

Massive stars, even though they have a short lifetime and are limited in number, are involved in many important phenomena in the universe. Massive stars help in chemical enrichment as they produce heavy elements in the universe (Maeder 1981; Wu et al. 2021; Higgins et al. 2023). They also drive star formation via different feedback mechanisms (Grudić & Hopkins 2019). Massive stars are bright and can be observed in other galaxies. This makes them an important tool for calibrating the distance scale (Pierce et al. 2000) as well. They are progenitors of supernovae, Wolf-Rayet stars, and sources of gravitational wave mergers, among many other products of stellar evolution. However, there remain issues in the theory of the evolution of massive stars that need improvement to fully understand the final products.

Current stellar evolution models for massive stars contains large theoretical uncertainties that are evident even in the main sequence phase. Since massive stars have radiative envelopes and convective cores, understanding the chemical mixing at the boundary of convective and radiative zones is important. Understanding chemical mixing also allows to probe changes main sequence lifetime and helium core masses, which propagates into compact remnant masses (Schootemeijer et al. 2019; Johnston 2021). Rotation in massive stars also impacts the evolution by inducing mixing, and mass loss (Maeder & Meynet 2000; Langer 2012; Hirschi et al. 2025). Magnetic fields adds another layer of complexity to the problem of evolution of massive stars (Keszthelyi et al. 2019, 2024). To tackle such problems, one needs many observables to break intrinsic parameter degeneracies.

Asteroseismology is an avenue to get observables for understanding the stellar interior. Asteroseismology with space-based photometry has improved our knowledge about stellar structure and the evolution of stars across the HR diagram (see reviews by Aerts 2021 and Kurtz 2022), from solar-type and red giant stars (Bedding et al. 2011; Huber et al. 2011; Miglio et al. 2012; Chaplin & Miglio 2013) to massive stars (Bowman 2020; Burssens et al. 2023). There are three main classes of pulsators: $\beta$ Cep stars, slowly pulsating B (SPB) stars, and stochastic low-frequency (SLF) variables (see Bowman 2023). While SPB stars are of somewhat lower masses ($3 \lesssim M \lesssim 9$ $M_\odot$), $\beta$ Cep stars allow us to probe stars with masses above about 8 $M_\odot$ and even upwards of 30 $M_\odot$ (Aerts et al. 2010; Bowman 2020). Stars with SLF variability are found over a range of stellar masses and may be explained by various mechanisms, different from that of SPB and

★ E-mail: a.moharana@keele.ac.uk, dr.ayush.moharana@gmail.com

© 2025 The Authors

$\beta$ Cep stars (Bowman 2023). $\beta$ Cep stars pulsate in pressure and gravity modes which are excited by the $\kappa$ mechanism within the Z-bump created by iron-peak elements (Dziembowski & Pamiatnykh 1993). The pulsation periods typically range from 2 to 8 h (Aerts et al. 2010; Bowman 2020). These high-amplitude pulsations have been found in massive stars across a wide range of masses and ages (Burssens et al. 2020; Fritzewski et al. 2025) and provide us a diverse sample to study massive stars.

Massive stars mostly exist in multiple systems (Sana et al. 2013; Duchêne & Kraus 2013; Offner et al. 2023). This further complicates the analysis of massive stars by adding complex phenomena like mass transfer and tidal effects (Podsiadlowski 2010; de Mink et al. 2014; Marchant & Bodensteiner 2024). Multiplicity also affects stellar pulsations, especially in close binaries (Guo 2021; Southworth & Bowman 2025). For example, mass transfer can change pulsation periods of both pressure and gravity modes (Wagg et al. 2024; Miszuda et al. 2025). Tidal forces can perturb the axis of pulsation during the course of the orbital motion (Bowman et al. 2019; Steindl et al. 2021; Van Reeth et al. 2023), and sometimes even tilt the pulsation axis (Fuller et al. 2020; Handler et al. 2022; Jayaraman et al. 2022). In specific cases, the tides from pulsations, known as inverse tides, can even influence the orbital motion (Fuller 2021). On the other hand, we can also use multiplicity to our advantage and increase the number and type of observables to constrain the uncertainties in our understanding of massive stars.

Double-lined eclipsing binaries (DLEBs) provide us with among the most precise direct measurements of stellar masses and radii (Torres et al. 2010). A pulsating star in a DLEB gives us the opportunity to connect the stellar structure with global stellar parameters. These systems have been documented in the literature since the 1970s (AB Cas; Tempesti 1971) but have been revolutionised because of space photometry — see review by Southworth & Bowman (2025). Early space-based missions like *MOST* (Walker et al. 2003), *CoRoT* (Baglin et al. 2006), and *Kepler* (Borucki et al. 2010; Howell et al. 2014) were highly successful for asteroseismology of low-mass stars but generally lacked $\beta$ Cep stars in EBs. While the *BRITE* mission (Weiss et al. 2014, 2021) did observe some bright $\beta$ Cep stars, the data quality was not as high as larger space missions. With the *Transiting Exoplanet Survey Satellite* (*TESS*; Ricker et al. 2015), the scene is changing with new discoveries of $\beta$ Cep in EBs (Southworth & Bowman 2022; Eze & Handler 2024). Still, to date there are only have five confirmed $\beta$ Cep stars in EB systems with precise mass and radius estimates[1] (Southworth 2015).

In this paper, we present a comprehensive analysis of V446 Cep, an EB with a $\beta$ Cep component. V446 Cep (RA=22:08:45.6, $\delta$=61:01:20.7) is a bright spectroscopic binary in the Alessi-Teutsch 5 open cluster. It was first discovered as an EB by Kazarovets et al. (1999) and its pulsating nature was first explored by Southworth & Bowman (2022). It was later analysed as a spectroscopic binary by Tkachenko et al. (2024), and is reported in the *TESS* catalogue of $\beta$ Cep stars in EBs by (Eze & Handler 2024). We combined ten sectors of *TESS* observations with high-resolution spectroscopy to provide precise stellar parameters of the EB, as shown in section 3. A comprehensive study of the pulsations is presented in section 4. We also found the presence of a stellar companion to the EB, which is described in section 5. Finally, we discuss the possible scenarios of formation and evolution of V446 Cep in section 6.

[1] DEBCat: https://www.astro.keele.ac.uk/jkt/debcat/

## 2 OBSERVATIONS

### 2.1 Spectroscopy

The spectroscopic observations included high-resolution Échelle spectra assembled with the high-efficiency and high-resolution Mercator Échelle spectrograph (HERMES; Raskin et al. 2011) mounted on the Mercator telescope at the Roque de los Muchachos Observatory on La Palma, Canary Islands, Spain. The HERMES spectrograph provides a high resolving power ($R \simeq 85\,000$ at 550 nm), and a large wavelength coverage from about 380 to 1000 nm.

In total, we use 72 HERMES spectra of V446 Cep. The reduction and rectification of these spectra prior to our work were described in detail in Tkachenko et al. (2024).

### 2.2 Photometry

The *TESS* mission was launched in April 2018 and is placed on an elliptical 13.70 d orbit around Earth. *TESS* has four wide-field-of-view CCD cameras which have a combined field of view of $24 \times 96$ deg$^2$. *TESS* observes a field (a sector of the whole sky) for about 27 d before changing the field. Over the years, some of the fields have been revisited by *TESS*, providing us with a long time base for the photometry of these fields.

V446 Cep (TIC 335265326) was observed across ten TESS sectors[2], specifically sectors 16, 17, 24, 56, 57, 76, 77, 83, 84, and 85. To check for possible contamination in the target pixel files (TPF) we used the code TPFPLOTTER[3] (Aller et al. 2020). TPFPLOTTER overlays nearby stars from the *Gaia* (Gaia Collaboration et al. 2016) on the TPF. The photometric aperture used by the *TESS* Science Processing Operations Center (SPOC; Jenkins et al. 2016) is also available to plot on the TPF as shown in Fig.1. We found that V446 Cep was the brightest star in the field. The only other star in the SPOC aperture was a star with a $G$-band brightness of $\sim$ 13 mag, compared to 7.8 mag for V446 Cep. Therefore we decided to use the simple aperture photometry (SAP) light curves with 2 min cadence, which are produced by SPOC.

We extracted the light curves from all sectors using LIGHTKURVE[4] (Lightkurve Collaboration et al. 2018). Long-term and short-term trends in the light curves were cleaned subsequently using the WOTAN[5] package (Hippke et al. 2019). The cleaning used the biweight time-windowed slider method (Mosteller & Tukey 1977). It involved two successive iterations with windows of 30 d and 8 d, respectively. We further removed parts of the light curve that did not have consistent eclipse depths by manual inspection. These were mostly incomplete eclipses near the gaps at the midpoint of each sector. This gave us the final light curve that we used for further analysis.

## 3 STELLAR PARAMETERS

We extracted the stellar, orbital, and atmospheric parameters of the binary system using a combination of photometric and spectroscopic analyses which are described in the following subsections.

[2] GI programmes: G022062, G06037, G06057, G05036, G05003
[3] https://github.com/jlillo/tpfplotter
[4] https://lightkurve.github.io/lightkurve/
[5] https://github.com/hippke/wotan

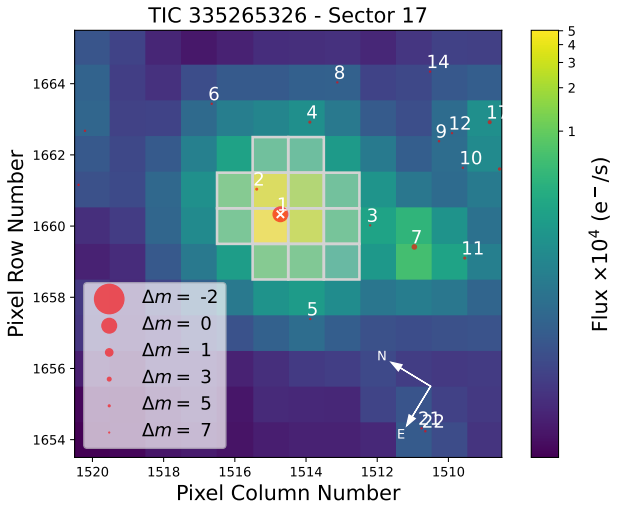


**Figure 1.** *TESS* TPF of V446 Cep with nearby sources. The marker sizes indicate the magnitude difference between V446 Cep and the respective star. Star 2 has a *G*-band magnitude of 13 compared to 7.8 of V446 Cep. The white lines mark the pixels used in the SPOC aperture.

### 3.1 Light curve modelling

#### *3.1.1* JKTEBOP

We used version 40 of the code JKTEBOP (Southworth 2013) for our modelling. We individually modelled light curves from every sector. We initialised our models with parameters from Southworth & Bowman (2022) and an approximate estimate of the time of primary minima ($T_0$) from the first primary eclipse of each sector. The initial set of free parameters included $T_0$, surface brightness ratio ($J$), sum of relative[6] radii ($r_1 + r_2$), radius ratio ($k$), eccentricity ($e_1$) and argument of periastron ($\omega_1$) parametrised as $e_1 \cos \omega_1$ and $e_1 \sin \omega_1$, orbital period ($P_1$), and light scale factor ($L_0$). We also optimised the fraction of reflected light on each star, which parametrised the reflection effect. The reflection effect is expected in such close systems with radiative atmospheres. After the first round of optimisation, we calculated the residuals after subtracting the binary model from the light curve. We found that additional polynomial fits were needed to remove some non-periodic trends that remained. These trends were shorter in time than the de-trending windows used before. JKTEBOP allows addition of polynomial fits to account for variation of any parameter in the model. We added polynomials to account for the variation of the total light of the system. We iteratively added polynomials to the model until we found the least residuals possible. We found that a good model only required two or three polynomials, without over-fitting any periodic trends. After optimisation of all the above parameters, we optimised the limb-darkening coefficients ($u_1$, $u_2$) and also the third light fraction[7] ($\mathrm{lf}_3$). The errors were calculated using the Monte Carlo (MC) algorithm available in JKTEBOP for 10000 iterations. The final residuals give us the pulsation light curve, which is shown in the bottom panel of Fig.2.

While JKTEBOP is excellent for modelling the binary contribution to the light curve, we found that $r_1 + r_2 = 0.31$, indicating that the stars are close enough to have deformations that are better modelled using Roche geometry. We only used the JKTEBOP model to extract the pulsation light curve as it was faster and easier to create an optimised binary model for all ten *TESS* sectors, compared to other binary modelling codes.

#### *3.1.2* PHOEBE2

To get a more accurate estimate of stellar parameters, we used the binary modelling code PHOEBE2[8] (Prša et al. 2016; Horvat et al. 2018; Jones et al. 2020; Conroy et al. 2020). The presence of high-amplitude (orbit-synchronised) pulsations may affect the measurement of a few parameters that are sensitive to the portions near the ingress and egress, for example, limb-darkening coefficients, and radius ratio. Therefore, such systems need joint modelling of the pulsations, the eclipse, and the Roche deformations. No such setup is currently available. Therefore, we removed the two pulsations with the highest amplitude using pre-whitening. We then modelled this pulsation-subtracted light curve using version 2.4.17 of PHOEBE2. We assigned the mean amplitude of the dominant pulsation as errors to the new pulsation-subtracted light curve. We used the light curve from the latest sectors: 83, 84, and 85. For computational efficiency, we randomly sampled the pulsation-subtracted light curve separately for eclipses and out-of-eclipse portions. We picked 1500 points from the eclipses and 500 from the out-of-eclipse portions. We phased this resampled, and pulsation-subtracted light curve over four orbital cycles and then proceeded to PHOEBE2 optimisation using the Nelder-Mead algorithm (Nelder & Mead 1965).

We used initial values of the stellar and orbital parameters from the JKTEBOP solutions. The irradiation model was set to the Horvat scheme (Prša et al. 2016). We set the gravity-darkening coefficients to the PHOEBE2 suggested values of unity. Reflection coefficients for both stars were set to unity. We started with the limb darkening setup from Southworth & Bowman (2022). We fixed the primary star temperature to the initial estimates from spectral analysis using eclipse spectra. The $a_1 \sin i_1$, and the mass ratio ($q_1$) were fixed to the estimates from the orbital solution from spectroscopy (see Table 2). After a loop of feedback between light curve modelling and spectroscopic analysis, we fixed the asynchronous rotation of the components (using the `syncpar` parameter) from the spectral analysis. We then sequentially optimised (in different runs) a set of parameters chosen from third light ($l_3$), $r_1 + r_2$, $e_1$, $\omega_1$, $i_1$, $k$, $T_{0,1}$, $P_1$, passband luminosity of the primary ($L_{\mathrm{pb},1}$), and the temperature ratio between the secondary star and the primary star ($T_{\mathrm{ratio}}$). The sequential optimisation was carried out until the root mean square (rms) of the residuals was less than 1 per cent of the total flux of the system. The final optimised model had residuals of rms less than 0.25 per cent of the total flux of the system (Fig.3). The errors were sampled using the Markov Chain MC algorithm implemented in PHOEBE2. We used 60 walkers for 10 parameters (see Table 1) and sampled it for 6000 chains with burn-in of 1000 chains. This sampling was carried out with a set of priors which included Gaussian distributions of effective temperature of the primary ($T_{\mathrm{eff},1}$), $P_1$, $q_1$, $a \sin i$, and uniform distributions of the `syncpar` parameter for both the primary and secondary companion. The final PHOEBE2 model is shown in Fig.3 and the MCMC corner plot can be found in Appendix A.

The final model gave us a $r_1 + r_2 = 0.31468^{+0.00047}_{-0.00039}$ and a $k = 0.2583^{+0.0015}_{-0.0017}$. We found a third light of 1.8 per cent of the total light. The primary and secondary contribute around 96.3 per cent and 1.9 per cent of the total light, respectively, with the secondary to

[6] defined relative to the semi-major axis ($a_1$)
[7] we define third light ($l_3$) as per Conroy et al. (2020)

[8] https://phoebe-project.org/

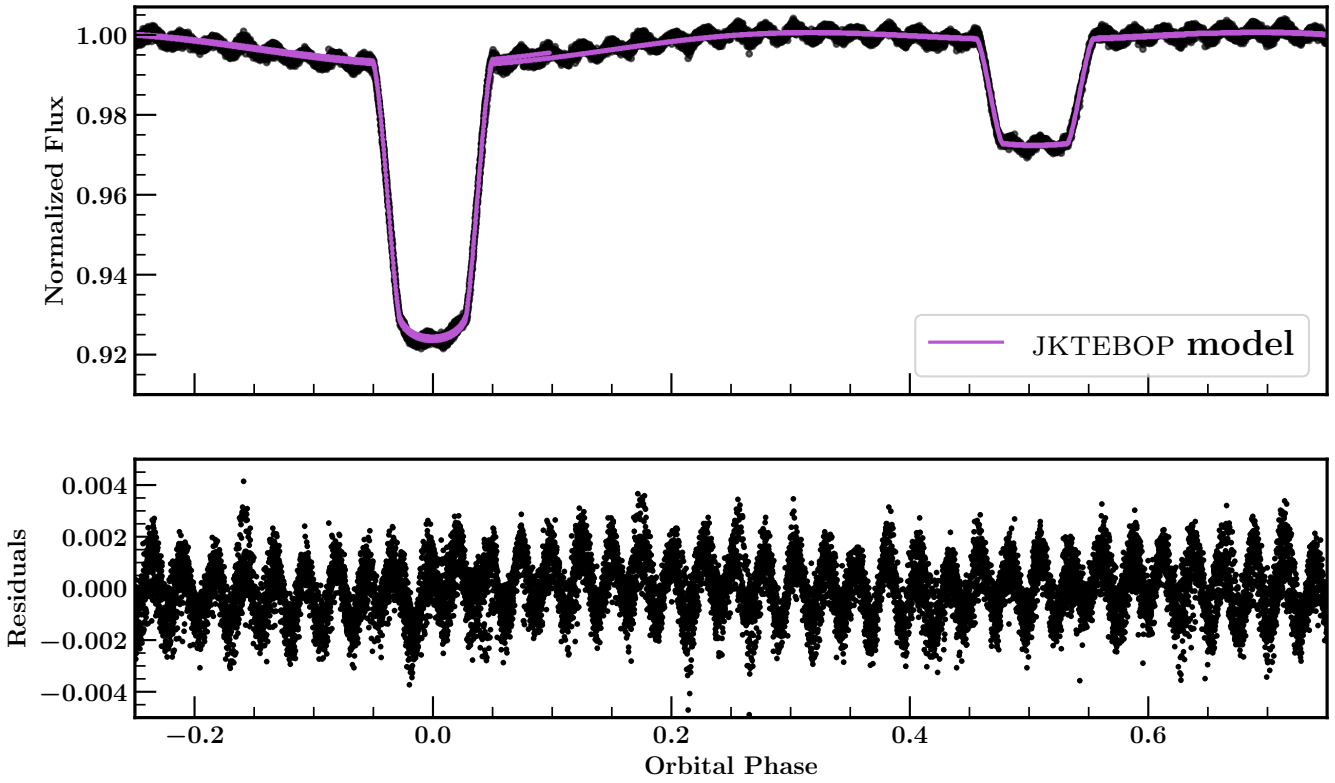


**Figure 2.** The top panel shows the binary phase-folded light curve and the binary model from JKTEBOP. The lower panel shows the residuals after subtraction of the binary model. The dominant pulsation ($\sim 10\,\mathrm{d}^{-1}$) is clearly visible and has around 39 cycles in one orbital phase.

primary light ratio being 0.0196. The final set of optimised parameters and their MCMC errors are given in Table 1.

To check for the consistency of the solutions, we used the final MCMC values as the starting values for a Nelder-Mead optimisation for the sectors 16, 24, 56, and 76. We subtracted the two dominant pulsations but did not resample these light curves. The light curves were optimised using Nelder-Mead for 150 iterations and involved the $P_1, T_{0,1}, r_1 + r_2, i_1, e_1, \omega_1, k$, $\mathrm{lf}_3$, and $T_{\mathrm{ratio}}$. The final estimates from the Nelder-Mead optimisation were assigned the errors from the MCMC sampling. We noticed deviation in values of the Nelder-Mead optimised parameters but no more than three per cent of their corresponding MCMC estimate, except $\mathrm{lf}_3$ where the MCMC estimate is less than half of the Nelder-Mead estimate. The difference could be due to a few number of iterations in the optimisation routine. Nonetheless, assuming that the MCMC errors were underestimated, we recalculated the parameter values and their errors by a weighted average of all the estimates: the Nelder-Mead estimates of sectors 16, 24, 56, 76, and the MCMC estimate. The MCMC estimate was assigned three times the weight compared to the Nelder-Mead estimates. The variation of the parameters are shown in Fig.4 and the final values of the parameters are listed in Table 1.

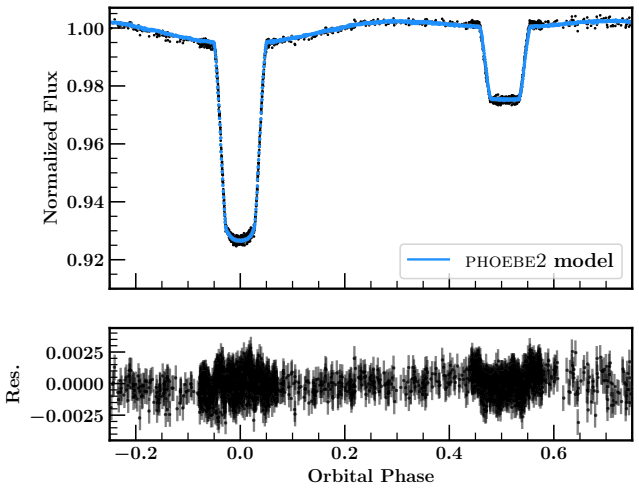


**Figure 3.** Phase-folded binary-LC (in black) with PHOEBE2 model (in blue). The bottom panel shows the residuals of the fit along with the error bars of the data points, in black.

### 3.2 Spectral disentangling and analysis

#### *3.2.1 Spectroscopic orbit*

The previous light curve (Southworth & Bowman 2022) and spectroscopic (Tkachenko et al. 2024) analyses made it clear that the secondary component in V446 Cep is a faint star, contributing barely

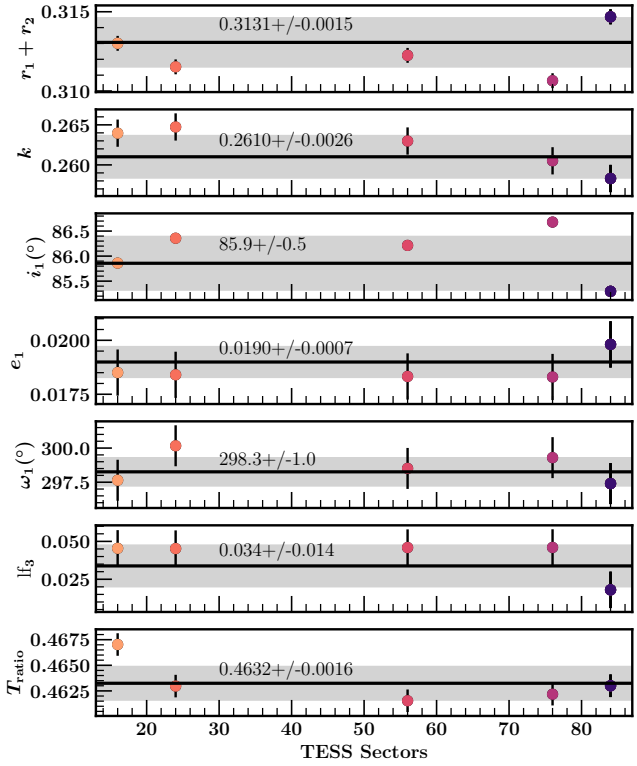


**Figure 4.** Variation of parameter values over different *TESS* sectors. The black points represent the MCMC estimate. The black line in every panel is the adopted value and the grey shaded region represents the range of the adopted errors of the corresponding parameters. Top to bottom: sum of fractional radii, radius ratio, binary inclination, eccentricity, argument of periastron, third light fraction, and ratio of effective temperatures.

2 per cent to the total light of the system. This was confirmed in our light curve analysis (c.f. subsection 3.1).

In this work, we employed the method of spectral disentangling (SPD; Simon & Sturm 1994; Hadrava 1995). SPD has some advantages for extracting spectra and radial velocities (RVs) in systems with two stars of different spectral types. First, there is no need for RV measurements as an input, hence any mismatches with template spectra are avoided. Second, the extracted spectra of the components do not assume any specific model template. This facilitates a detailed atmospheric analysis of the components. SPD is also a powerful method for the detection of faint component(s) in high contrast systems. Component(s) contributing only a few per cent to the total light of the system have been successfully detected using SPD (Mayer et al. 2013; Torres et al. 2014; Kolbas et al. 2015; Themeßl et al. 2018; Johnston et al. 2023). This method has also been successful in cases where the spectral lines are almost washed out due to high rotational velocity and their depth is less than 1 per cent of the normalised continuum (Pavlovski et al. 2022).

One of the fundamental requirements of SPD is that there should be no intrinsic line profile variations (LPVs) in the spectra of the components, except for the dilution effect in the course of the orbital cycle. Such a variation can be due to the Rossiter-McLaughlin effect (Kopal 1959), which makes the spectra during the ingress and egress phases of an eclipse unreliable. In our sample of HERMES spectra, 33 were obtained during an eclipse. These spectra were not used in SPD, making the sample substantially smaller. Another source of LPVs is

**Table 1.** PHOEBE2 setup, priors, and the final parameters. The setup includes the PHOEBE2 parameters corresponding to the limb darkening law, the two coefficients corresponding to the law, bolometric fraction of incident light that is reflected, coefficient for gravity darkening corrections, and the passband luminosity mode. The priors are included from the spectroscopic estimates where the PHOEBE2 parameters for asynchronicity are calculated from the spectroscopic estimates of rotational velocities and the expected synchronised velocity. More details about the PHOEBE2 parameters are available at: `https://phoebe-project.org/docs/2.4/physics`.

| Parameter | Value |
|---|---|
| Fixed parameters | |
| `ld_mode` | 'quadratic' |
| `ld_coeffs@primary` | [0.094, 0.232] |
| `ld_coeffs@secondary` | [0.2, 0.238] |
| `irrad_frac_refl_bol`[a] | 1 |
| `gravb_bol`[a] | 1 |
| `pblum_mode` | 'component-coupled' |
| Priors | |
| $P_1$ [d] | 3.808567 ± 0.00005 |
| $T_{\rm eff,1}$ [K] | 24220 ± 200 |
| $q_1$ | 0.1550 ± 0.0012 |
| $a_1 \sin i_1$ [$R_\odot$] | 23.555 ± 0.05 |
| `syncpar@primary` | 1.81 ± 0.2 |
| `syncpar@secondary` | 3.15 ± 0.3 |
| Fitted and sampled parameters | |

| | MCMC estimate | Final value |
|---|---|---|
| $T_0$ [BJD - 2457000] | $3610.34690^{+0.00074}_{-0.00083}$ | 3610.344 ± 0.005 |
| $e_1$ | $0.01981^{+0.00107}_{-0.00097}$ | 0.0190 ± 0.0007 |
| $i_1$ [deg] | $85.296^{+0.091}_{-0.095}$ | 85.9 ± 0.5 |
| $\omega_1$ [deg] | $297.4^{+1.5}_{-1.4}$ | 298.3 ± 1.0 |
| $r_1 + r_2$ | $0.31468^{+0.00047}_{-0.00039}$ | 0.3131 ± 0.0015 |
| $k = r_2/r_1$ | $0.2583^{+0.0017}_{-0.0015}$ | 0.2610 ± 0.0026 |
| $L_{\rm pb,1}$ [W] | $12.27^{+0.13}_{-0.15}$ | $12.27^{+0.13}_{-0.15}$ |
| $l_3$ [Wm$^{-2}$] | $0.018^{+0.014}_{-0.010}$ | - |
| $lf_3$ | $0.018 \pm 0.012$[b] | 0.034 ± 0.014 |
| $T_{\rm ratio}$ | $0.4630^{+0.0011}_{-0.0011}$ | 0.4632 ± 0.0016 |

[a] For all components
[b] Propagated from $l_3$ and $L_{\rm pb}$

pulsations. Since V446 Cep contains a $\beta$ Cep pulsating component, this is relevant in our analysis. It was found in practice that small line profile distortions due to non-radial modes would not seriously affect the RV curves (Tkachenko et al. 2012, 2014; Lehmann et al. 2013; Themeßl et al. 2018; Johnston et al. 2023) but if also radial pulsations are involved, another strategy in SPD is needed (Tkachenko et al. 2016; Pilecki et al. 2021).

For SPD we used the code FDBINARY (Ilijic et al. 2004) which is based on disentangling in Fourier space (Hadrava 1995) but implements a discrete Fourier transform (DFT). This enables more reliable handling of the input data. The methodology of SPD and subsequent atmospheric analysis adopted in the present work is extensively described in Pavlovski et al. (2018, 2023).

After some trials with short spectral segments with a width ~ 100 Å, which did not return any stable solutions, a longer segment spanning $\lambda$ = 4180 - 5150 Å was adopted for the determination of the

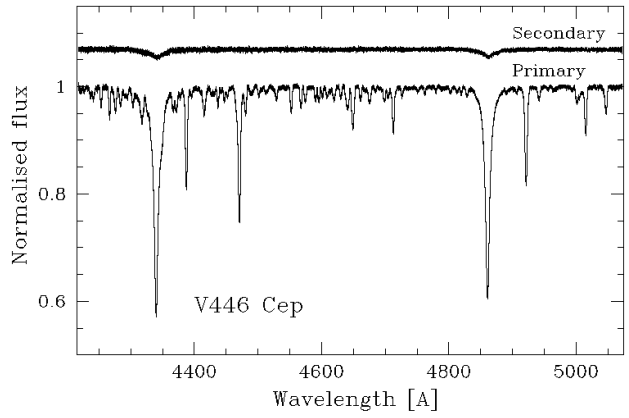


**Figure 5.** The spectra of the components in V446 Cep as reconstructed by SPD. Disentangled spectra are still in a common continuum of a binary system; hence, the highly diluted secondary component is obvious.

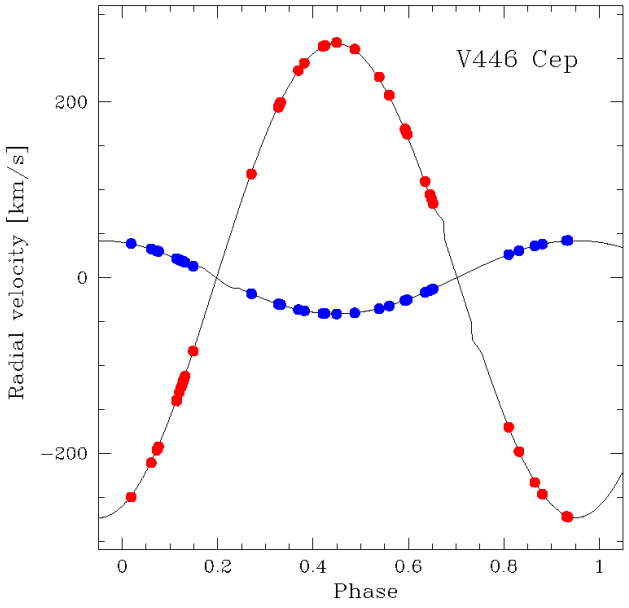


**Figure 6.** The solution for the spectroscopic orbit from SPD is represented in solid lines. The phase distribution of the observed spectra is illustrated with blue (primary) and red (secondary) circles. In SPD the orbital parameters are directly optimised by-passing the RVs for individual exposures - therefore symbols are only for illustrative purposes. The Rossiter-McLaughlin effect in the course of the primary and secondary eclipses is seen in the computed solution.

spectroscopic orbit with SPD. This segment includes two Balmer lines, H$\gamma$ and H$\beta$, some He I lines, and numerous metal lines that are typical of early B-type stellar spectra. The projected rotational velocity of the primary component is high. As a consequence, the overlapping of spectral lines and line blends is present in the observed spectra. Usually, we avoid intrinsically broad Balmer lines in the determination of the orbital parameters: (i) the width of Balmer lines in B-type stars is larger than the RV changes for a given component, and (ii) broad Balmer lines in hot stars are usually extended to

**Table 2.** Optimal parameters of the spectroscopic orbit determined by SPD. The period $P$ was fixed with the value found from the initial light curve solution. All other parameters of the orbit, time of periastron passage ($T_{\rm per}$), $e_1$, $\omega_1$, and the RV semi-amplitudes for both components, $K_1$ and $K_2$ were left free. $q_1$, $M_1$ sin$^3$ $i$ and $M_2$ sin$^3$ $i$ and the semimajor axes $a$ sin $i$, calculated from the optimised parameters, are given.

| Parameter | Unit | Value |
|---|---|---|
| Determined | | |
| $P_1$ | [d] | 3.808574 (fixed) |
| $T_{\rm per}$ | [d] | 55701.01±0.11 |
| $e_1$ | - | 0.0133±0.0021 |
| $\omega_1$ | [deg] | 74.0±9.8 |
| $K_1$ | [km s$^{-1}$] | 42.02±0.32 |
| $K_2$ | [km s$^{-1}$] | 271.05±0.49 |
| Calculated | | |
| $q_1$ | - | 0.1550±0.0012 |
| $M_1$ sin$^3$ $i_1$ | M$_\odot$ | 10.603±0.057 |
| $M_2$ sin$^3$ $i_1$ | M$_\odot$ | 1.644±0.017 |
| $a_1$ sin $i_1$ | M$_\odot$ | 23.555±0.044 |

multiple Échelle orders. Proper normalisation of the observed spectra is challenging and could be a source of systematic errors in the determination of the orbital parameters. But in our case, we needed to resort to Balmer lines for the faint companion. The light curve solution suggested that the secondary component is either a late B-type or an early A-type star with the effective temperature ($T_{\rm eff}$) around 11 000 K. Thus, its Balmer lines are almost at maximal strength. This gave us a much better prospect for extracting the secondary spectra compared to the metal lines which are rather weak and not numerous, except for Mg II line at 4481 Å. The use of Balmer lines for the secondary was proven to be a good decision since the spectrum of the secondary component was revealed to have Balmer line depths of only 1.5 per cent of normalised flux, whilst depths of metal lines were found to be less than 0.3 per cent and are hidden in the noise (Fig.5). The parameters of the spectroscopic orbit are given in Table 2. The uncertainties of the orbital parameters are calculated with a bootstrap technique as implemented in Pavlovski et al. (2018).

The only spectroscopic orbits for V446 Cep in the literature are from Tkachenko et al. (2024). The agreement between our study and Tkachenko et al. (2024) is satisfactory except that the RV semi-amplitude of the secondary component ($K_2$) differs considerably. It is hard to trace the source of this inconsistency because the same observed spectra and the same disentangling code were used in both studies. However, we only used the 40 out-of-eclipse spectra. Hence, we suppose that the eclipse spectra (33 in both eclipses) might be the primary source for a large discrepancy in $K_2$ of almost 40 km s$^{-1}$. The selection of the spectral segment could also contribute to the discrepancy, as the line profiles vary substantially for different wavelength ranges (see Appendix B for examples).

While the values of $e_1$ we determined in SPD (0.1330 ± 0.0021) are within 1-$\sigma$ uncertainty of the value found in the light curve analysis (0.0190 ± 0.0007), the discrepancy in $\omega_1$ between these two complementary solutions is large and hard to explain. In fact, $\omega_1$ is the most uncertain quantity in the spectroscopic solution. Apsidal motion, in spite of a very small eccentricity, might be a source of strong disagreement because of different epochs of the observations. Moreover, a 10-year gap between the observing seasons in which the spectra were obtained might be another reason for a large error in spectroscopic determination of $\omega_1$.

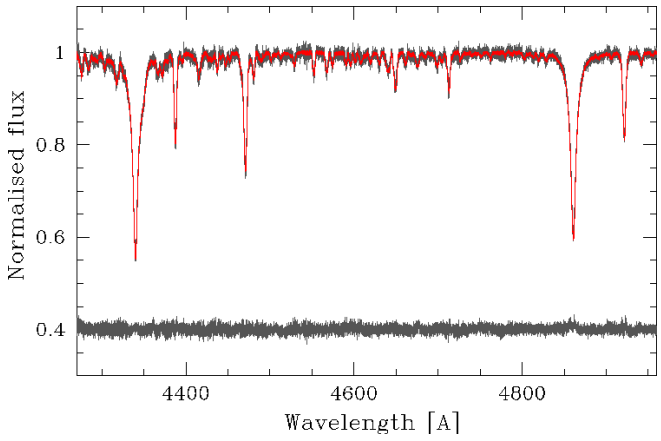


**Figure 7.** Disentangled spectrum of the primary component (in red) superimposed on the primary's spectrum (in black) obtained in the total eclipse. The residuals are also shown, and shifted by 0.4 in the units of the normalised continuum for convenience.

In context of possible apsidal motion in V446 Cep we noticed that $\zeta$ Phe, an intermediate mass binary system has very similar eccentricity, $e = 0.0116 \pm 0.0024$ (Southworth 2020) and one of the fastest apsidal motion with $\dot{\omega} = 6.16 \pm 0.20$ deg yr$^{-1}$, corresponding to the period $U = 58.4 \pm 1.8$ yr (Zasche & Wolf 2007). The fastest apsidal motion was found in GL Car with $\dot{\omega} = 14.29 \pm 0.03$ deg yr$^{-1}$, and $U = 25.20 \pm 0.02$ yr with a higher eccentricity (Wolf et al. 2008). An apsidal motion of $\dot{\omega} \sim 22$ deg yr$^{-1}$ would explain the $\omega_1$ discrepancy in V446 Cep, but such a fast apsidal motion was not detected in the eclipse timing variations (ETVs; see subsection 5.1). But the ETVs point at variations of the time of periastron which could be a reason for the discrepancy. We did a check for a SPD solution with an additional companion but could not get a solution. Sometimes there is an ambiguity between solutions differing by $\pm\pi$. Unfortunately we can not resolve the discrepancy for our results with certainty.

### 3.2.2 *The primary's spectrum in the total eclipse*

The secondary eclipse in the light curve of V446 Cep is total with the primary (i.e. hotter and brighter) component eclipsing its companion. This allows direct comparison of the primary's spectrum with its disentangled spectrum. Most of the eclipse spectra were obtained in the phases of ingress or egress of the eclipses, but two of the spectra are very close to midpoint of the total eclipse. These two spectra resemble each other, so we decided to co-add them to enhance the signal-to-noise ratio (S/N).

The disentangled spectrum of the primary component is diluted, and for direct comparison to the eclipse spectrum, the light ratio should be known. We turned this around and determined the light ratio by varying it until these two spectra match, minimising the sum of the squared residuals. This gave us $l_s/l_p = 0.022 \pm 0.004$, which is in excellent agreement with the light curve analysis. The slight difference could be due to the wavelength dependence of the light ratio since the spectra belong to the blue spectral region whilst *TESS* is sensitive to redder wavelengths. The comparison of the scaled disentangled spectra and the eclipse spectra is shown in Fig.7. No conspicuous trends in the residuals are noticeable.

Since SPD co-adds all observed spectra, the disentangled spectra of the components gain in S/N. We measured S/N in a short spectral segment free of the spectral lines from 4570 Å to 4580 Å, the region of the Si III triplet. This yielded S/N = 670 for the primary's disentangled spectra compared to the S/N of 155 for the eclipse spectra.

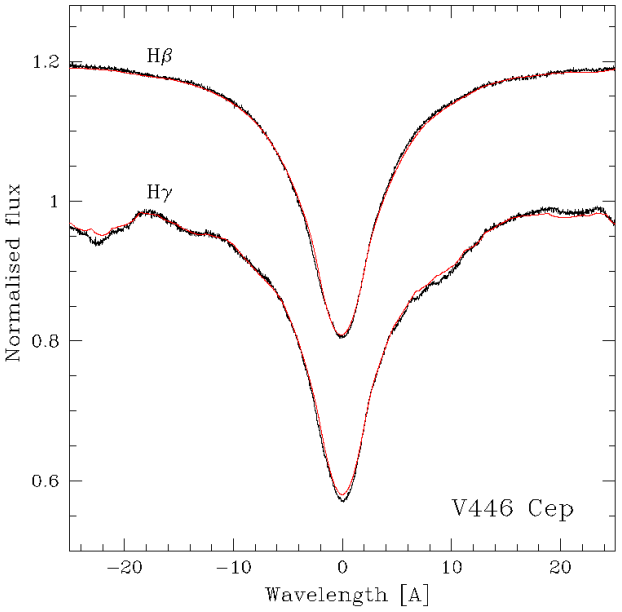


**Figure 8.** Optimal fits (in red) of the H$\gamma$ and H$\beta$ in the disentangled spectrum of the primary component of V446 Cep (in black). In fitting the disentangled spectrum, metal lines superimposed on the wings of the Balmer lines were masked. The log $g$ and the light ratio were fixed from the solution of the light curve analysis.

**Table 3.** Atmospheric parameters determined for the components of the binary system V446 Cep.

| Parameter | Unit | Primary | Secondary |
|---|---|---|---|
| Constrained | | | |
| $T_{\rm eff}$ | [K] | 23830±260 | 9080±390 |
| log $g$ | [cgs] | 3.91 (fix) | 4.30 (fix) |
| lf | | 0.978±0.006 | 0.022±0.003 |
| $v \sin i_1$ | [km s$^{-1}$] | 143.2±3.0 | 64.1±6.3 |
| Eclipse | | | |
| $T_{\rm eff}$ | [K] | 24220±180 | |
| log $g$ | [cgs] | 3.91 (fix) | |
| lf | - | 1.0 (fix) | |
| $v \sin i_1$ | [km s$^{-1}$] | 142.5±2.9 | |

### 3.2.3 *Atmospheric parameters*

The light curve analysis and the spectroscopic orbit gave us multiple constraints for our spectroscopic analysis. For example, hydrogen lines are excellent indicators of the $T_{\rm eff}$ with the drawback that for stars with $T_{\rm eff} > 8\,000$ K, a strong degeneracy appears with the surface gravity (log $g$). However, the log $g$ of the components of DLEBs can be measured with high precision. Thus, we lifted the degeneracy between the $T_{\rm eff}$ and log $g$ by fixing log $g$ in our estimation.

The spectrum of the primary component was also characterised

by using its strong He I lines, specifically for constraining $T_{\rm eff}$. They were also useful for the determination of the projected rotational velocity ($v$ sin $i$), which cannot be defined from the Balmer lines only. We also found one weak line of He II at 4686 Å which gave an upper limit to the primary's $T_{\rm eff}$. In the spectrum of the secondary component, only the H$\gamma$ and H$\beta$ Balmer lines were clearly visible due to its very low flux contribution. They had a depth of less than 2 per cent of the normalised continuum, with metal lines hardly recognisable in the noise. The renormalised spectrum of the secondary component yielded S/N $\simeq$ 14. Further, the large difference in the $T_{\rm eff}$ of the components meant that we had to use two grids of the theoretical spectra, one with local thermodynamic equilibrium (LTE) approximation for the secondary component, and the other with non-LTE (NLTE) assumption for the primary component.

The code STARFIT (Kolbas et al. 2015) was used in the determination of the optimal atmospheric parameters for the components of V446 Cep. In STARFIT, the disentangled and renormalised spectrum are compared to pre-calculated theoretical spectra. The optimisation is performed using a genetic algorithm with the subroutine AMOEBA (Charbonneau 1995). The uncertainties are calculated with MCMC sampling (Foreman-Mackey et al. 2013). Details on the grids with theoretical LTE spectra are given in Kolbas et al. (2015), and for NLTE spectra in Pavlovski et al. (2018, 2023). Both grids are calculated for solar metallicity, [M/H]= 0, which eventually limits the scope of our results.

In our calculations, the metal lines in the primary's disentangled spectrum were masked, along with the wings of H$\gamma$ and H$\beta$ lines. For the secondary's disentangled spectrum, we fit only spectral segments with a width of about 80 Å and centred on the H$\gamma$ and H$\beta$ lines. Spectral fitting is performed in a constrained mode with fixed values of log $g$ for both components. The atmospheric parameters obtained and the light dilution factors[9] are given in Table 3. The quality of the best fit is shown in Fig.8 for the primary's H$\gamma$ and H$\beta$ lines, respectively. We also fit the eclipse spectra to check for any difference arising from our method of renormalising disentangled spectra. We find that, even with much lower S/N than in the primary's disentangled spectrum, the eclipse spectra give similar parameters, which corroborates within the quoted 1-$\sigma$ uncertainties (Table 3).

Finally, we note that the $v$ sin $i$ for both components, $v_1 \sin i_1 = 143.2 \pm 3.0\,{\rm km\,s^{-1}}$ and $v_2 \sin i_1 = 64.1 \pm 6.3\,{\rm km\,s^{-1}}$, are substantially larger than the synchronised rotational velocities inferred from the components' radii, which are $v_1 \sin i_{1,\rm syn} = 76.8 \pm 0.3\,{\rm km\,s^{-1}}$ and $v_2 \sin i_{1,\rm syn} = 19.9 \pm 0.1\,{\rm km\,s^{-1}}$, respectively.

### 3.2.4 *Abundances*

The high S/N of the disentangled spectrum of the primary component allowed us to determine the individual abundances for several atomic species in its photosphere. Its early-B type characteristics mean that the lines of C , N , O , Mg and Al are mostly present in a single ionisation stage.

A hybrid NLTE model approach was adopted where modelling combines hydrostatic, plane-parallel, and line-blanketed model atmospheres in LTE with line formation calculated in NLTE (Nieva & Przybilla 2007, 2012). The ATLAS9 code (Kurucz 1979; Castelli & Kurucz 2003) was used in the calculations of model atmospheres. Then emergent fluxes and line profiles were calculated with the codes DETAIL and SURFACE (Giddings 1980; Butler 1984). In DETAIL, coupled radiative transfer and statistical equilibrium equations were solved, while SURFACE was used for the calculations of NLTE synthetic spectra. The model atoms used were the result of a dedicated critical evaluation by K. Butler (Munich), N. Przybilla (Innsbruck), and their associates over decades, with the most recent list of references for different ions given by Aschenbrenner et al. (2023).

In the calculation of the model atmosphere for the primary component, we set $T_{\rm eff}$ = 23830 K and log $g$ = 3.91. The grid of synthetic spectra was calculated for different abundances in steps of 0.05 dex, and microturbulent velocity $\xi$ in steps of 1 km s$^{-1}$. Finally, the calculated spectra were broadened by a rotational profile with $v \sin i = 143\,{\rm km\,s^{-1}}$. The least scatter in oxygen abundance was found for $\xi = 4 \pm 1\,{\rm km\,s^{-1}}$, which is then used in abundance determination for other species. The results of abundance determination is given in Table 4. The abundance of helium is not determined since we used the helium lines in the determination of the $T_{\rm eff}$. In the model atmosphere for the primary, the He abundance was set to the standard value log $\epsilon$(He) = 0.089 by number of atoms. We found that abundance patterns in V446 Cep are consistent with those of OB binaries (Pavlovski et al. 2018, 2023) and even single B-type stars (Nieva & Przybilla 2012). We could not extract the abundance of the secondary as we had limited lines.

The final set of stellar, orbital, and orbital parameters that we adopt are given in Table 5. We use the light curve estimates for $P_1$,$T_{0,1}$,$i_1$, $e_1$, and $\omega_1$, while we adopt the spectroscopic mass ratio. $i_1$, $k$, and $r_1 + r_2$ from light curve solution were used with the spectroscopic solution to obtain the stellar parameters. We adopted the $T_{\rm eff}$ and $v\sin(i_1)$ from the eclipse spectra for the primary. The only possible direct measurement of the secondary's $T_{\rm eff}$ and $v\sin(i_1)$ was available from the disentangled spectra.

**Table 4.** Elemental abundances for the primary component of V446 Cep. The mean values found for the sample of 22 stars in OB binaries from Pavlovski et al. (2018, 2023) and for 'present-day cosmic abundances' of single sharp-lined early B-type stars determined by Nieva & Przybilla (2012) are given for comparison. The number in square brackets represents the number of lines considered for the analysis.

| Element | V446 Cep A | No. of lines | OB binaries | B-type stars |
|---|---|---|---|---|
| log $\epsilon$ (C) | 8.16±0.11 | 7 | 8.25±0.07 | 8.33±0.04 |
| log $\epsilon$ (N) | 7.68±0.10 | 21 | 7.69±0.06 | 7.79±0.04 |
| log $\epsilon$ (O) | 8.67±0.12 | 15 | 8.71±0.05 | 8.76±0.05 |
| log $\epsilon$ (Mg) | 7.60±0.09 | 2 | 7.56±0.12 | 7.56±0.05 |
| log $\epsilon$ (Si) | 7.33±0.16 | 3 | 7.45±0.09 | 7.50±0.05 |
| log $\epsilon$ (N/C) | -0.48±0.15 | - | -0.56±0.08 | -0.54±0.06 |
| log $\epsilon$ (N/O) | -0.99±0.13 | - | -1.02±0.07 | -0.97±0.06 |

## 4 FREQUENCY ANALYSIS

### 4.1 Frequency extraction

We created the pulsation light curve by stitching the residuals from sectors 16-85 after JKTEBOP modelling. This resulted in a dataset of 128,537 points and a timebase of 1846 d. We used DFT and extracted the pulsation frequencies using PERIOD04 (Lenz & Breger 2005). We looked in the frequency range between 0 and 30 d$^{-1}$. In an initial check, we did not find any frequencies beyond this range with sufficient S/N that were recurrent in all sectors. Hence all our analyses are confined in this range. We extended the search beyond the suggested S/N limit for TESS data (Baran & Koen 2021) to search for low-amplitude multiplets, if present. We extracted all significant

[9] with the condition $l_1 + l_2 = 1$

**Table 5.** Adopted parameters of the V446 Cep binary system. We adopt $e_1$, and $\omega_1$ from the light curve solution. $a_1$ was calculated from $a_1 \sin i_1$ obtained using SPD, and $i_1$ from light curve solution.

| Orbital Parameters | |
|---|---|
| | A–B |
| $T_{0,1}$ [BJD - 2457000] | 3610.34690(83) |
| $P_1$ [d] | 3.808567(12) |
| $a_1$ [$R_\odot$] | 23.62(5) |
| $i_1$ [deg] | 85.9(5) |
| $e_1$ | 0.0190(7) |
| $\omega_1$ [deg] | 298(1) |
| $q_1$ | 0.1550(12) |
| **Stellar and atmospheric parameters** | |
| | A B |
| $M$ [$M_\odot$] | 10.68(6) 1.657(17) |
| $R$ [$R_\odot$] | 5.864(33) 1.530(14) |
| $T_{\rm eff}$ [K] | 24220(180) 9080(390) |
| $\log(g)$ [dex] | 3.946(5) 4.303(9) |
| $v\sin(i_1)$ [km s$^{-1}$] | 143(3) 64(6) |
| $u_1$ | 0.094 0.200 |
| $u_2$ | 0.232 0.237 |
| lf (light curve) | 0.947(17) 0.019(12) |
| lf (spectroscopy) | 0.978(6) 0.022(3) |
| Fractional radii | 0.2483(13) 0.0648(6) |
| $T_{\rm ratio}$ light curve | 0.4632(16) |
| $T_{\rm ratio}$ spectroscopy | 0.375(19) |
| **System parameters** | |
| [M/H] [dex] | 0 (assumed) |
| Age [Myr] | 14.5(5) |
| $lf_3$ | 0.034(14) |
| Distance [pc] | 750.0[a] |

[a] From SED (see section 6).

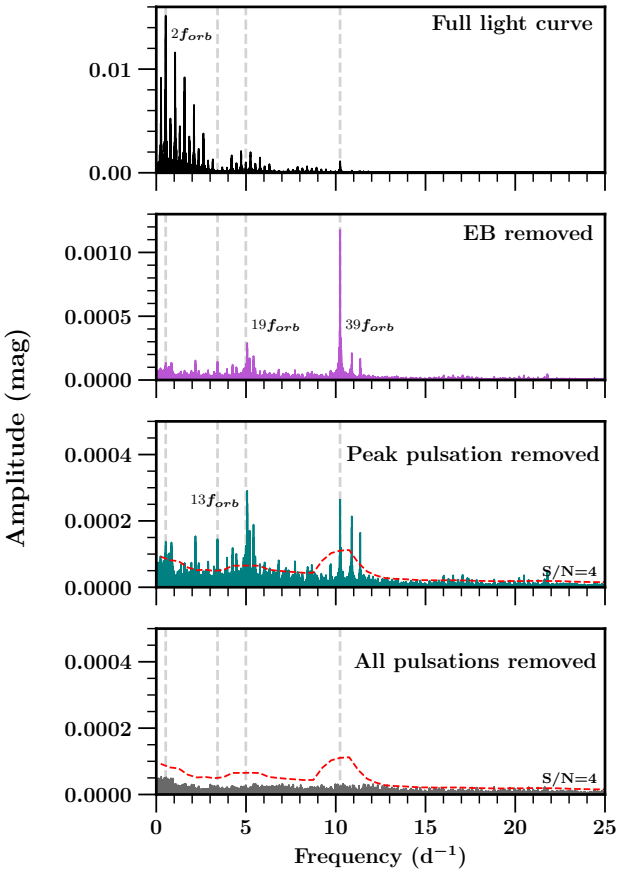


**Figure 9.** DFT of the light curves for different stages of frequency extraction. The top panel shows the DFT (in black) of the full *TESS* light curve with eclipses. The panel second from the top (in purple) shows the DFT of eclipse eclipse-subtracted light curve. The second from the bottom (in green) is the pre-whitened DFT after the removal of the dominant pulsation frequency. The bottom-most panel shows the pre-whitened DFT after the removal of all 142 pulsations. The grey lines denote different harmonics of the orbital frequency. The red dashed line shows the limit for an S/N of 3.

frequencies with iterative pre-whitening until we reached the S/N criterion of 4 (Fig.9).

There were long gaps in the total light curve but four sets of consecutive sectors were available. To check for the consistency of the frequency solution, we divided the light curve into sets of the consecutive sectors: 16-17, 56-57, 76-77, and 83-85. We compared the frequency spectrum for these sets and checked for recurrent frequencies and rule out binary signatures and aliases. We accepted or rejected frequencies based on the methodology detailed in Appendix C. This gave us 21 recurrent frequencies. The final set of frequencies is listed in Table 6. We checked if these frequencies are harmonics of the orbital frequency ($f_{\rm orb}$) or combinations of each other. Using the Rayleigh criterion of 0.012 d$^{-1}$, we found only 3 such possibilities as listed in Table 6.

### 4.2 Line-profile variations

In an attempt to identify the pulsation modes $f_1$ and $f_2$, we tried to check for LPV using the HERMES spectra. Mode identification from spectroscopy using LPVs involves analysing the amplitude and phase changes across stellar spectral lines as a function of velocity or wavelength. The intensity period search (IPS; Telting & Schrijvers 1997) method enables the construction of diagnostic diagrams by fitting periodicities at each pixel of the stacked spectra, allowing the determination of pulsation mode quantum numbers ($\ell$, $m$) by comparing observed amplitude and phase distributions with model predictions. This technique has been successfully applied in various pulsating stars, including $\beta$ Cephei and slowly pulsating B stars (e.g., Telting & Schrijvers 1997; Briquet et al. 2003, 2012; Aerts et al. 2010). The phase behaviour across the line profile is a key diagnostic, as it encodes the azimuthal order $m$, distinguishing between zonal, prograde, and retrograde modes (Telting & Schrijvers 1997).

Our dataset comprises 72 spectra with a median temporal sampling of approximately 0.12 d$^{-1}$, corresponding to a Nyquist frequency limit near 4.2 d$^{-1}$, compared with the most prominent pulsation frequencies found from *TESS*, i.e., $f_1$ = 10.24324 d$^{-1}$ and $f_2$ = 5.06430 d$^{-1}$. This Nyquist limit imposes a physical constraint beyond which frequency information is aliased, complicating the interpretation of pulsation modes. Although methods exist to extract information above the Nyquist limit under exceptional conditions (e.g., high signal-to-noise space-based data; Kallinger et al. 2008;

**Table 6.** Final set of extracted pulsation frequencies, which are listed in order of decreasing amplitude. We also list the closest orbital harmonic to each frequency in terms of N, where the harmonic frequency is N×$f_{\rm orb}$. Possible combination frequencies are also listed in the table.

| No. | $f$ ($d^{-1}$) | Amplitude ( mmag) | Phase (rad) | S/N | N | $f - N \times f_{\rm orb}$ | Remarks |
|---|---|---|---|---|---|---|---|
| $f_1$ | 10.2432419(5) | 1.20(1) | 0.201(2) | 46 | 39 | 0.0030(3) | - |
| $f_2$ | 5.064302(2) | 0.30(1) | 0.618(5) | 20 | 19 | 0.0755(2) | - |
| $f_3$ | 10.893687(2) | 0.23(1) | 0.069(7) | 10 | 41 | 0.1283(3) | - |
| $f_4$ | 5.417558(3) | 0.18(1) | 0.435(8) | 12 | 20 | 0.1662(2) | - |
| $f_5$ | 11.362614(3) | 0.17(1) | 0.400(9) | 11 | 43 | 0.0721(4) | - |
| $f_6$ | 5.201641(3) | 0.16(1) | 0.779(9) | 11 | 19 | 0.2128(2) | - |
| $f_7$ | 2.182762(3) | 0.15(1) | 0.82(1) | 12 | 8 | 0.08220(7) | - |
| $f_8$ | 4.251804(4) | 0.12(1) | 0.93(1) | 8 | 16 | 0.0507(1) | - |
| $f_9$ | 4.952164(6) | 0.09(1) | 0.41(2) | 6 | 18 | 0.2259(1) | - |
| $f_{10}$ | 7.730014(6) | 0.09(1) | 0.69(2) | 9 | 29 | 0.1155(2) | - |
| $f_{11}$ | 4.866921(7) | 0.08(1) | 0.76(2) | 5 | 18 | 0.1407(1) | - |
| $f_{12}$ | 6.318200(8) | 0.07(1) | 0.48(2) | 6 | 24 | 0.0165(2) | - |
| $f_{13}$ | 7.231708(8) | 0.06(1) | 0.86(3) | 6 | 27 | 0.1423(2) | - |
| $f_{14}$ | 3.41200(1) | 0.05(1) | 0.52(4) | 5 | 12 | 0.2612(1) | - |
| $f_{15}$ | 7.06233(1) | 0.05(1) | 0.05(3) | 5 | 26 | 0.2355(2) | - |
| $f_{16}$ | 7.20783(1) | 0.05(1) | 0.31(3) | 5 | 27 | 0.1184(2) | $f_{10}$-$2f_{\rm orb}$ |
| $f_{17}$ | 2.75414(1) | 0.05(1) | 0.11(3) | 4 | 10 | 0.12844(8) | - |
| $f_{18}$ | 8.57942(1) | 0.04(1) | 0.56(4) | 4 | 32 | 0.1772(3) | - |
| $f_{19}$ | 21.78854(1) | 0.04(1) | 0.20(4) | 10 | 82 | 0.2578(7) | $2f_3$ |
| $f_{20}$ | 20.48212(2) | 0.03(1) | 0.84(5) | 9 | 78 | 0.0017(6) | $2f_1$ |
| $f_{21}$ | 17.39559(3) | 0.02(1) | 0.07(8) | 5 | 66 | 0.0660(5) | - |

Murphy et al. 2013), ground-based spectroscopy of moderate quality generally cannot surpass this threshold reliably. Despite these limitations, one may still yield insights by focusing on trends in amplitude and phase rather than their absolute values.

Some spectral lines, such as the Si III triplet near 4552 Å or Si II doublet near 4130 Å, are well-known diagnostics of pulsations in early-type stars due to their sensitivity to velocity fields induced by stellar oscillations (e.g., Briquet et al. 2003, 2005). However, these lines tend to be weak, and often suffer from blends with neighbouring lines, especially with the close N II line at 4552.53 Å, which complicates accurate continuum normalization and reduces confidence in the extracted amplitude and phase signals (De Ridder et al. 2002). Consequently, analysis of these lines demands high-resolution and high signal-to-noise data. By contrast, the He I 4026 Å line, although less sensitive to pulsations than Si III, is more sensitive to changes in temperature. He I 4026 Å line is typically stronger and less affected by blends, making it a more robust tracer of pulsation LPVs in noisy datasets (Briquet 2003). Since the Si III lines form in deeper layers of the stellar atmosphere than He I, they are more sensitive to the vertical structure of the pulsation velocity field. As a result, differences in phase and amplitude behaviour between these lines may arise and can provide insights into the deep structure of both vertical and horizontal components of the pulsation velocity field.

We corrected the spectra for the systemic velocity ($\gamma = -19.266$ km s$^{-1}$) and smoothed-out line profiles for 50 consecutive points in case of the Si III triplet and for 100 points in case of the He I line. Next, in each pixel of the stacked spectra we fitted the orbital frequency $f_{\rm orb} = 0.263\,{\rm d}^{-1}$ with the two dominant pulsation frequencies, i.e. $f_1 = 10.24324\,{\rm d}^{-1}$ and $f_2 = 5.06430\,{\rm d}^{-1}$, to correct for orbital motion and to extract amplitude and phase variations across the line profiles. The resulting amplitude and phase distributions across the line profiles are shown in Fig.10. Each of the upper panels presents the amplitude variations for the pulsation frequencies, with the corresponding phase distributions shown below. The normalised mean line profiles are also shown for reference.

From the above-mentioned reasons regarding the Nyquist limit, we follow the analysis based mainly on the phase variations of the frequencies. In our dataset, the He I line (left panels of Fig.10) shows that the amplitude for frequency $f_2$ shows a single peak centred in the line, while the phase remains approximately constant across the entire line profile. The absence of any phase gradients or jumps, combined with the centrally peaked amplitude, suggests a radial mode ($\ell = 0$, $m = 0$). However, when examining the same frequency in the Si III lines (middle and right panels of Fig.10), the phases exhibit a smooth and monotonic decrease from blue to red wings. This is a hallmark of a prograde non-radial mode ($m > 0$), as the travelling wave induces a Doppler shift that results in a smooth phase gradient, and thus contradicts the interpretation based on the He I line.

In contrast, the behaviour of $f_1$ is ambiguous and must be interpreted with caution. In the He I line, the amplitude remains non-zero throughout the profile, and the phase exhibits no coherent or interpretable trend, preventing any reliable mode identification. Both Si III lines exhibit amplitude minima near the line centre. In the Si III 4552.62 Å line, the phase remains approximately constant and close to zero, marginally consistent with a low-degree zonal mode ($m = 0$), though uncertainties in the line core are large. In the Si III 4567.872 Å line, a sharp phase change is observed at the location of amplitude minimum, a feature that could be indicative of a zonal non-radial mode ($\ell > 0, m = 0$), where the projected velocity field changes sign across the stellar disk. However, given the substantial uncertainties in the IPS maps and the lack of consistent trends across lines, these features should be regarded as suggestive rather than conclusive.

Taken together, these results indicate that $f_2$ may be associated with a non-radial prograde mode ($m > 0$), while $f_1$ could correspond to a non-radial, zonal mode ($\ell > 0, m = 0$). However, these interpretations are tentative due to the limited spectral resolution, moderate signal-to-noise ratio, and the small number of observations. The differing phase behaviours observed between the He I and Si III lines further highlight the influence of line formation depth and local atmospheric conditions on the observed pulsation signatures.

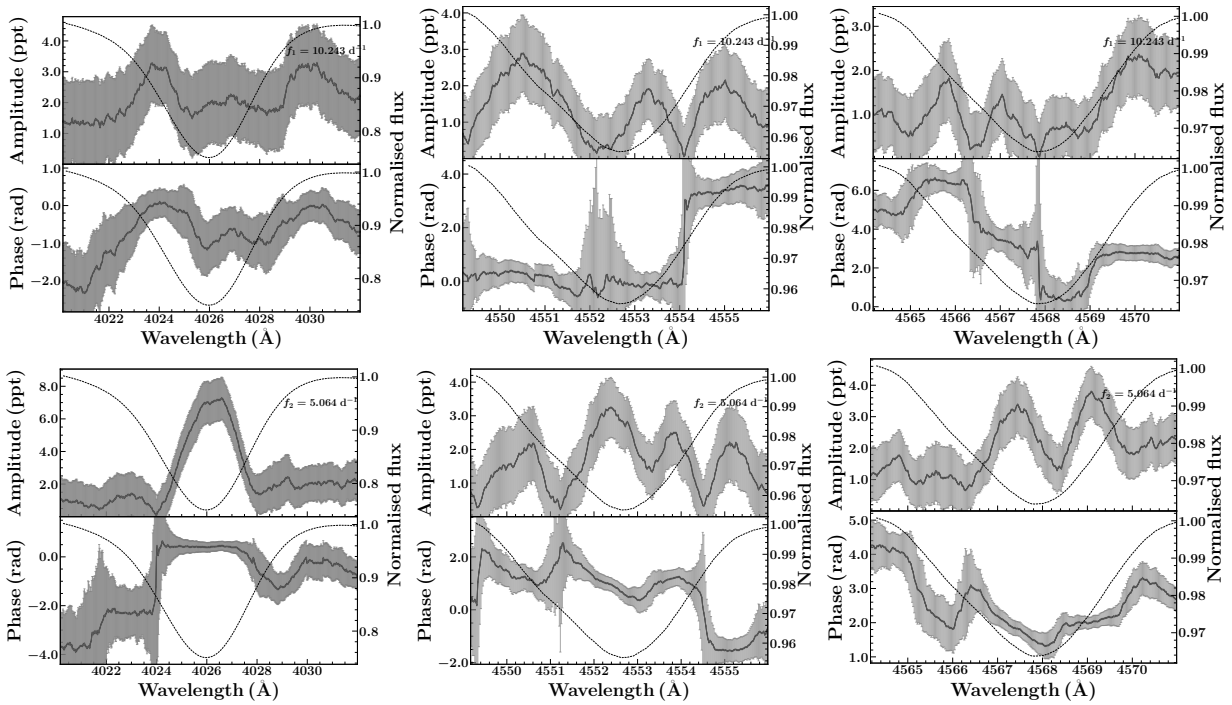


**Figure 10.** LPVs for $f_1$ (top panels) and $f_2$ (bottom panels) for different lines. From left-to-right: He I 4026.191 Å, Si III 4552.62 Å and Si III 4567.872 Å lines. The LPVs are in black with the errors shown as the grey shaded region. The smooth dotted curve represents the mean line profiles and are given for reference.

### 4.3 Tracing tidal effects

The dominant pulsation frequency is a near-harmonic of the orbital frequency ($f_1 = 39 f_{\rm orb} + 0.003\ \mathrm{d}^{-1}$) and is visible in the phase-folded residuals of the JKTEBOP light curve fitting, shown in Fig.2. This near-harmonic frequency could be a result of possible interaction between the stars and the pulsation. To check if this frequency is tidally perturbed, we need to observe variation in the mode's amplitude and phase over the orbital motion. We look for amplitude and phase variation of this frequency by following an approach similar to Steindl et al. (2021). We divided the pulsation light curve into small segments that corresponded to 21 divisions of the orbital phase. We then fit the small segments separately with the function

$$A(t) = A_0 \sin\left(2\pi(f_i t + \phi)\right) + c_0\ , \qquad (1)$$

where we fix the frequency $f_i$, and fit for the amplitude $A_0$, and $\phi$ of each segment, and $c_0$ is the zero-point shift in the amplitude of the fit. We use the Levenberg–Marquardt algorithm to fit for the parameters with constraints on $\phi$ to vary from 0 to 1. The $A_0$ and $\phi$ variations for $f_1$ and $f_2$, as a function of orbital phase ($\Phi$), are shown in Fig.11. We notice that $f_1$ has low amplitudes at both eclipses. But these amplitude variations are small in scale and therefore do not provide any strong evidence of tidal perturbation. The phase does not even vary slightly over the orbital phase. Meanwhile, for $f_2$, we do not see any variations in either amplitude or phase.

To check for tidal perturbation of the other pulsation frequencies, we created an Échelle diagram where the frequencies were phased with the $f_{\rm orb}$ (Fig.12). We found no multiplets which have similar Échelle phases and are separated in frequency by multiples of the $f_{\rm orb}$. We did find the rejected frequencies (in grey in Fig.12) to show multiplets, but they can be due to improper binary modelling or eclipse mapping of some modes. Unfortunately, with their low amplitudes, it is difficult to conclusively trace their origin.

Fuller et al. (2020) showed that the amplitude variations of tidally trapped pulsations are dependent on the pulsating star's $R/R_{\rm Roche}$. To place V446 Cep in the context of other pulsating close binaries with tidal effects, we consider the Roche-filling factor ($R/R_{\rm Roche}$) of the current sample of these systems from Kurtz et al. (2020); Steindl et al. (2021); Southworth et al. (2020, 2021); Van Reeth et al. (2022, 2023); Rappaport et al. (2021); Jayaraman et al. (2022, 2024); Johnston et al. (2023); Kurtz et al. (2020); Jennings et al. (2024), and Zhang et al. (2024). We used estimates of the orbital periods, masses, and radii of the stars from the literature and then used PHOEBE2 to construct a binary model to calculate `requiv_max`, which is the $R_{\rm Roche}$, for each star. We found that most of the tidally perturbed systems had the pulsating component within $1\sigma$ of the $R/R_{\rm Roche}$ value of 0.69, which is shown in Fig.13. Interestingly, V446 Cep A lies just at the edge of this limit. The other stars below V446 Cep A, in Fig.13, are V446 Cep B, and a K star of mass 0.66 $M_\odot$ which is not pulsating. This further contributes to the argument that V446 Cep A is not a tidally perturbed system.

The dominant pulsation frequency of V446 Cep A is almost an exact harmonic of the $f_{\rm orb}$. It is not impossible to have such a coincidence, given that the density of pulsation frequencies is high in $\beta$ Cep stars. But V446 Cep is half way through its tidal synchronisation time and is tens of mega years away from circularisation (see section 6) and therefore, will have changes in the orbital frequency. It is possible that its dominant pulsation was or will become an exact harmonic of the orbital frequency.

In Fig.13, the stars labelled as tidally trapped pulsators (see Southworth & Bowman 2025) have two components with large values of $R/R_{\rm Roche}$. On the other hand, the values of $R/R_{\rm Roche}$ does not appear to distinguish the tidally tilted pulsators and the non-tilted pulsators. This could hint that other intrinsic factors affect the coupling of tides and pulsations, therefore, it needs further exploration. To calculate

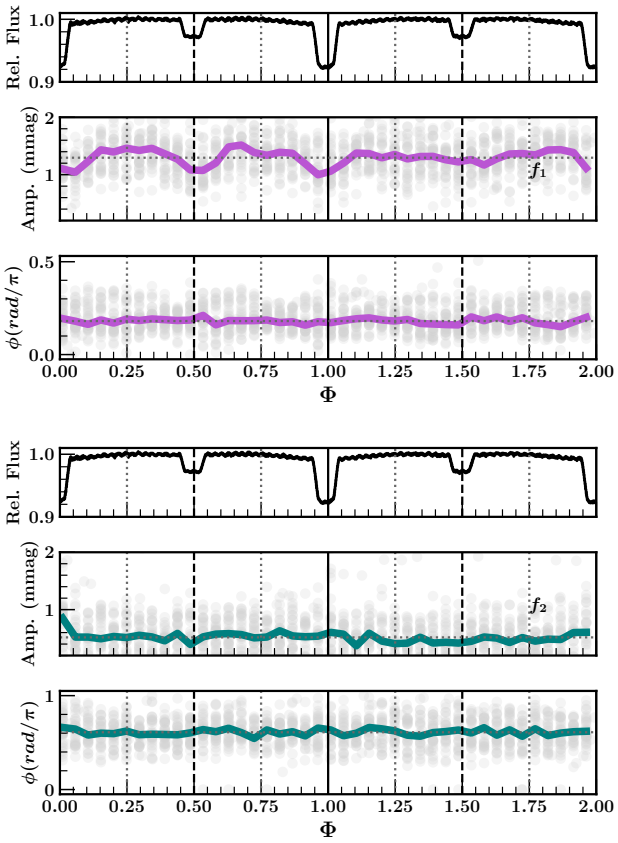


**Figure 11.** Pulsation runs for $f_1$ (top; purple), and $f_2$ (bottom; green). The dominant pulsation frequency, $f_1$, has slight amplitude variations at primary and secondary eclipses, but not substantial enough to confirm tidal perturbation.

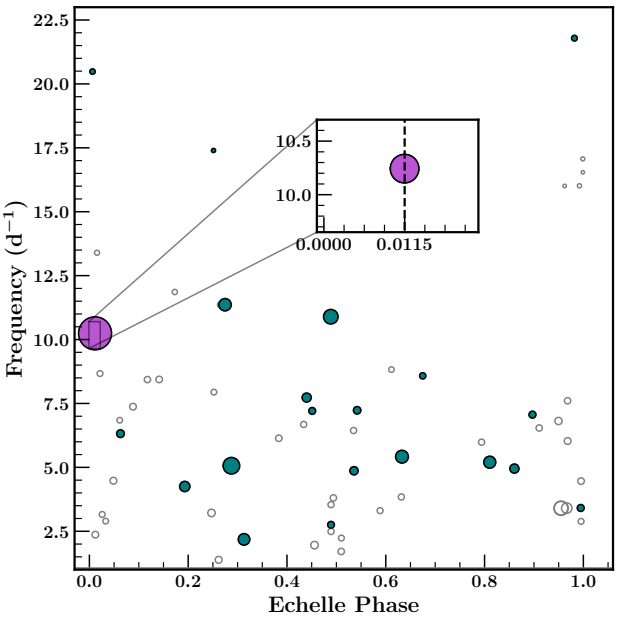


**Figure 12.** Échelle diagram of the final set of extracted pulsation frequencies. The Échelle phase has been calculated for the orbital frequency. The marker size for the frequencies is proportional to their amplitude. The dominant pulsation frequency is marked in purple, the final set of frequencies is marked in green, and the grey circles are frequencies that were rejected in our analysis.

$R/R_{\rm Roche}$, one needs both mass and radius for the pulsator and, therefore, such pulsators in EBs will prove invaluable.

## 5 THIRD BODY

V446 Cep has long-term proper motion changes, which were visible in *Hipparcos* and in *Gaia* second and third data releases (DR2 and DR3; Kervella et al. 2019; Brandt 2021). In Kervella et al. (2019), V446 Cep was identified as an astometric binary but with a primary mass of 6.348 $M_\odot$ and a "AU-normalised" secondary mass of 363.42 $M_J$ or 0.346 $M_\odot$. This estimation uses equation 7 in Kervella et al. (2019):

$$\frac{m_2}{\sqrt{a}} = \sqrt{\frac{m_1}{G}} v_1 \,, \tag{2}$$

where $m_1$ and $m_2$ denote the primary and secondary masses, respectively, $a$ is the orbital radius, and $v_1$ is the tangential velocity anomaly calculated in Kervella et al. (2019). Using values for $m_1$ and $a$ from our work, we derive $m_2 = 0.149$ $M_\odot$. Both the estimates are quite small compared to our measured value for $m_2$. This could mean that the orbit (and the companion) identified in Kervella et al. (2019) is that of a tertiary companion.

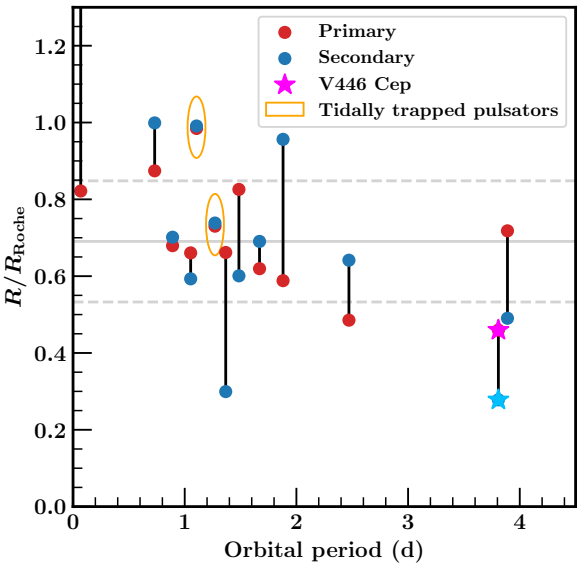


**Figure 13.** Roche-filling factors ($R/R_{\rm Roche}$) versus orbital periods for different tidally perturbed systems with mass and radius measurements in the literature. V446 Cep is marked with a star. The grey lines show the mean and standard deviations for the Roche-filling factors of all pulsators (both secondary and primary, in case the source of pulsation is not identified) in the sample.

### 5.1 Eclipse timing

In order to confirm the presence of the tertiary component, we applied the timing procedure developed by Marcadon & Prša (2024) to the *TESS* 2-minute cadence data of V446 Cep. We adopted the phenomenological model of Mikulášek (2015), which analytically describes the eclipse profile as

$$f(t_i, \Theta) = \alpha_0 + \sum_{k=1}^{n_e} \alpha_k \, \psi(t_i, T_k, d_k, \Gamma_k, C_k), \tag{3}$$

where $\alpha_0$ is the flux zero-point shift, $n_e$ is the number of eclipses during one cycle, and $\alpha_k$ is a scaling coefficient of the eclipse profile function, which is written as

$$\psi(t_i, T, d, \Gamma, C) = \left\{1 + C\left(\frac{t_i - T}{d}\right)^2\right\} \times \left\{1 - \left\{1 - \exp\left[1 - \cosh\left(\frac{t_i - T}{d}\right)\right]\right\}^{\Gamma}\right\}. \tag{4}$$

Here, $T$, $d$, $\Gamma$, and $C$ are the time of minimum, the eclipse width, the kurtosis, and the scaling parameter, respectively. For each individual eclipse, the time of minimum is estimated as

$$\begin{aligned} T_k &= T_{0,k} + PE + \Delta_k \\ &= T_{0,k} + P \times \mathrm{round}\left(\frac{t_i - T_{0,k}}{P}\right) + \Delta_k, \end{aligned} \tag{5}$$

where $T_{0,k}$, $P$, $E$, and $\Delta_k$ are the reference time of eclipse, the orbital period, the epoch, and the observed minus calculated ($O-C$) time difference, respectively. Additionally, the out-of-eclipse variability can be taken into account by including the contribution of the O'Connell and proximity effects in Eq. (3), as described by Marcadon & Prša (2024).

In the first step, we performed a MCMC fit of each sector's light curve assuming that the eclipses are strictly periodic (i.e., $\Delta_k = 0$ for each eclipse). For each sector, we obtained a set of parameters that best fit the corresponding light curve from a chain of $10^5$ iterations. Given that the light curve of V446 Cep is stable with time (no evidence of activity-induced variability is found), we adopted the set with the smallest value of normalised $\chi^2$, among the 10 single-sector light curves, as reference. In the second step, we generated a chain of $10^4$ iterations for each available sector, leaving $\Delta_k$ as a free parameter and fixing the other parameters to their best-fitting values. Finally, we calculated the times of minima from the best-fitting values of the parameter $\Delta_k$ using equation (5) and removed those occurring during data gaps. The times of minima derived from our fitting procedure are listed in Table E1 in Appendix E, along with the errors representing $1\sigma$ percentiles from the MCMC posteriors.

### 5.2 Period Changes

The amplitude of the dominant pulsation, $f_1$ is around 2.5 per cent of the primary eclipse, 6.7 per cent of the secondary eclipse, and 400 per cent of the frequency with the second highest amplitude.

To complement the eclipse timing method for detecting a tertiary component, we investigated the period variations of the dominant pulsation frequency of V446 Cep to search for signatures of the light-travel time effect (LTTE,; Irwin 1952, 1959). Our objective was to apply a Fourier-based, modified Hertzsprung method (see e.g. Hajdu et al. 2021; Rodríguez-Segovia et al. 2022) to derive the $O-C$ variations. The detailed methodology is outlined in Rathour et al. (2024, 2025). Each *TESS* sector, with carefully subtracted eclipse signatures, served as the starting point of the analysis. We removed all significant frequencies except the dominant mode at $f_1 \simeq 10.24324$ d$^{-1}$. Once the overall data were cleaned for additional signals, we investigated for period change behaviour of the dominant pulsation frequency $f_1$. Unlike the eclipse timing technique, which measures the timing of individual eclipses, the Hertzsprung method tracks phase shifts of the pulsation light curve relative to a reference template that is constructed from a Fourier fit to the light curve. The comparison of any given observed light curve segment with the template results in a phase shift over time, hence providing a direct measure of a period change (see e.g. Bowman et al. 2016, 2021). Uncertainties for individual $O-C$ points were estimated using a bootstrap resampling approach (see Hajdu et al. 2021).

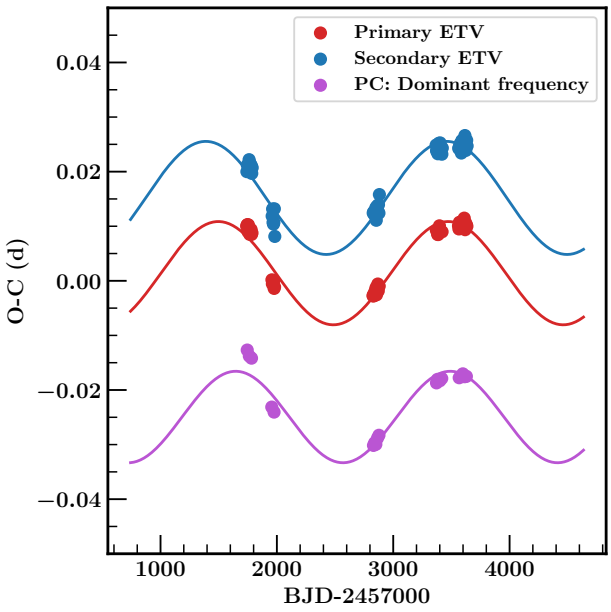


**Figure 14.** Timing variations for primary eclipses (in red), secondary eclipses (in blue), and the period change (PC) of the dominant pulsation frequency (in purple; shifted for clarity). The lines show sinusoidal fits with a period corresponding to 2310 days.

The resulting $O-C$ diagram derived from period change analysis and the ETVs, corresponding to both the primary and secondary eclipses, is shown in Fig.14. It shows sinusoidal variations with a period of about 2310 d and an amplitude of 0.15 d, indicating the presence of a tertiary stellar companion. The coherent time variations from the two different methods means that the source of eclipses and the pulsation is the same. Therefore, we confirm that the pulsation originates from the binary system and is not a result of contamination in the large *TESS* pixels.

### 5.3 Combining radial velocities

Using traditional RV extraction methods, we found it difficult to extract the faint secondary. But we were able to extract the primary RVs both using broadening functions (BF; Rucinski 1992) and two-dimensional cross-correlation (TODCOR; Zucker & Mazeh 1994) methods. These RVs were similar to the RV time series we extracted using SPD. We also fit the RVs from the BF method with a binary model and used the residuals to search for the tertiary companion.

To get a better coverage of the orbital phase of the outer orbit,

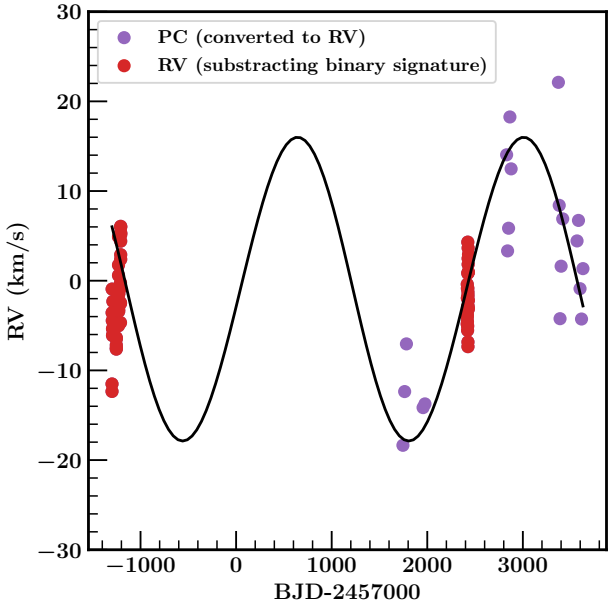


**Figure 15.** Joint RV-PC fit for the tertiary (in black). The RVs (in red) and PCs (in purple) are spread over a period of around 5000 d while the tertiary is in an orbit of 2408 d.

**Table 7.** Tertiary parameters estimated from v2fit and gaiamock.

| Parameter | Value |
|---|---|
| $P_2$ [d] | 2408.44 ± 0.01 |
| $T_{0,2}$ [d] | 2458222.385 |
| $e_2$ | 0.0 |
| $i_2$ [deg] | 90 ± 10 |
| $\Omega_2$ [deg] | 0 to 360 |
| $f_2$ | 0.1± 0.025 |
| $a \sin i_2$ [AU] | 8.212 ± 0.240 |
| $K_3$ [km s$^{-1}$] | 12.5 ± 1.7 |
| $M_3 \sin^3 i_2$ [M$_\odot$] | 4.23 ± 0.46 |
| Angular size [mas] | 18 ± 3 |

we combined these RVs with the pulsation-derived timing variations (i.e. $O-C$) converted into an equivalent RV curve. We transformed the $O-C$ points into RV using:

$$v_{\rm rad} = c\frac{{\rm d}\tau}{{\rm d}t} \tag{6}$$

where $c$ is the speed of light and $\tau = (O-C) \times 86400.0$ denotes the LTTE delay in seconds. The time derivative, ${\rm d}\tau/{\rm d}t$, was evaluated numerically using a finite-difference gradient method.

Using this joint RV-PC dataset, we used v2fit (Konacki et al. 2010) to fit for the tertiary star. The resulting fitting parameters are in Table 7. The orbital fit is shown in Fig.15. Unfortunately, the scatter of the RVs was large, and the orbital phase coverage was poor. They were slightly helpful in constraining the outer orbital period ($P_2$). Nonetheless, we found the projected mass of the tertiary ($M_3 \sin^3 i_2$) to be 4.23 ± 0.46 M$_\odot$.

### 5.4 Comparison with astrometric simulations

To better understand the configuration of the companion, we use gaiamock[10] (El-Badry et al. 2024) to simulate the system with different configurations of the tertiary orbit. gaiamock also calculates the *Gaia* re-normalised unit weight error (RUWE) for a certain configuration of orbital parameters like the masses, period, sky-inclination ($i_2$), longitude of the ascending node ($\Omega_2$) of the orbit of a system, and flux-ratio of the system ($f_2$). In our case, we treat the eclipsing binary as a single star and the whole system as a binary. Therefore, the gaiamock setup was initialized as a 12.34 M$_\odot$ primary and a secondary star with a mass of $4.23/\sin^3 i_2$ M$_\odot$.

We simulated different models of this binary with different combinations of $i_2$, $f_2$, and $\Omega_2$ and kept fixed the parallax, orbital period, and eccentricity. For these models, we calculated $\Delta_{\rm RUWE}$ defined as:

$$\Delta_{\rm RUWE} = |{\rm RUWE}_{Gaia} - {\rm RUWE}_{\rm mod}| \tag{7}$$

where RUWE$_{\rm mod}$ is calculated from gaiamock and RUWE$_{Gaia}$ is the value from *Gaia* DR3. From this grid of models, we picked models that had the lowest $\Delta_{\rm RUWE}$. Then, we looked at the distributions of $i_2$, $f_2$, and $\Omega_2$ for the models with $\Delta_{\rm RUWE}$ less than 0.3 (Fig.16). This limit was estimated from a sample of close triple systems with known orbital parameters (see Appendix D). There were 20 such models compared to the total sample of 128 000, which we identify as the most probable solutions. We find that these models had $i_2$ of 90 ± 10° and f$_2$ around 0.1. There was no obvious preference for $\Omega_2$. The model with the lowest $\Delta_{\rm RUWE}$ (0.22) has $i_2 = 90 \pm 10°$ , $f_2 = 0.04 \pm 0.15$, and $\Omega_2 = 20 \pm 20°$, where the errors represent the bin size of each parameter. Only $f_2$ is different from the most probable solution. The most probable configuration gives us a tertiary with a mass of 4.23 M$_\odot$. An $i_2$ around 90° means that the system is co-planar and therefore there is a possibility of observing extra eclipses in the system. With the estimated $T_{0,2}$, we expected extra eclipses in *TESS* sectors 83 to 85. Unfortunately, we found no such eclipses. We also calculated the angular size of the system with errors calculated assuming an error of 150 pc in the *Gaia* distances. The orbital parameters of the tertiary are listed in Table 7.

## 6 EVOLUTION AND FORMATION

The inner binary of V446 Cep has a low mass-ratio. If the system was formed this way, it presents an interesting case to study the formation of close binaries in massive stars. Another possible scenario is that mass transfer in the past changed the configuration of the system from a higher mass ratio to a smaller mass ratio. We found no evidence of mass transfer in the abundance patterns. To shed more light, we decided to check if the system is co-evolving. The parameters of the newly found tertiary companion also need to be taken into consideration to get the whole picture of the evolutionary state of the system.

We use spectral energy distribution (SED) for expected multiple-star configurations to constrain the stellar parameters of the companion. For this, we use the Python routine SEDfit[11]. SEDfit allows fitting a multiple-star SED, assuming a single metallicity for the whole system, by querying archival photometric fluxes in ultraviolet, visible, and infrared bands. We fit an SED to three possible cases for the system: (i) A binary with a compact object (no additional stellar

[10] https://github.com/kareemelbadry/gaiamock
[11] https://github.com/mkounkel/SEDFit

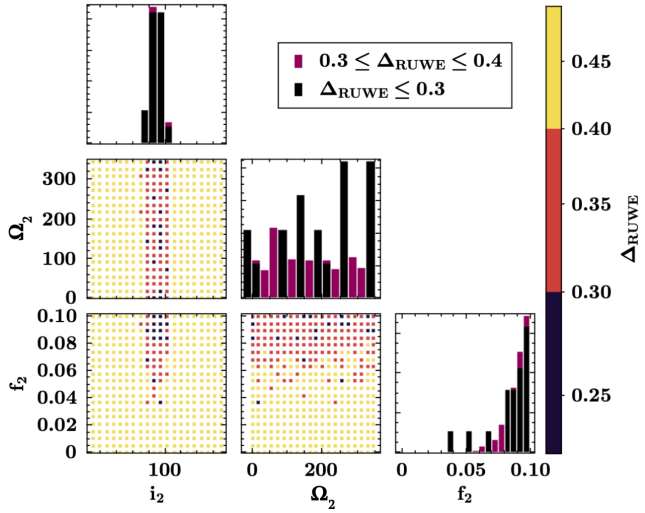


**Figure 16.** Distribution of $\Delta_{\rm RUWE}$ for GAIAMOCK models with different values of $i_2$, $f_2$, and $\Omega_2$. The models in black have $\Delta_{\rm RUWE} < 0.3$ and represent the physically feasible models.

flux from the companion) (ii) A triple system with a main-sequence star (where we expect flux from the third star) and (iii) A quadruple system where the eclipsing binary is orbited by another binary (consisting of similar stars). We fix the radius, $\log g$, $T_{\rm eff}$ of the binary stars from the light curve modelling and spectroscopic analysis. The metallicity was set to zero with a range of variation set from -0.05 dex to 0.05 dex. For the companion(s), we set an initial search range of 0.5 $R_\odot$ to 3 $R_\odot$ in radius, 3.5 dex to 4.6 dex in $\log g$, and 2000 K to 10,000 K in temperature. We then changed the ranges separately for case-(ii) and case-(iii) to get a best fitting solution which gave the mass/combined mass close to $4.23 \pm 0.20\,M_\odot$. The final fits are shown in Fig.17. After we get SED parameters from the fitting, we use the expected mass, radius, and temperature of the companion, and the EB, to estimate the age. We do this by fitting isochrones from MESA Isochrones and Stellar Tracks (MIST; Choi et al. 2016; Dotter 2016). With these constraints, we discuss the possible formation and evolution of the system below.

### 6.1 Tertiary is a compact object

We find that case-(i) (left panel of Fig.17) keeps the system at a distance of 731.6 pc, compared to the reported *Gaia* distance of 900 pc. This could mean that either the tertiary is a black hole or a close neutron-star binary (due to the maximum mass limit for neutron stars). We see third-light in the light curve solution, which acts against accepting this scenario, but that could also arise from other complementary structures, e.g., accretion disks. If the system hosts a compact object, one would expect that the tertiary underwent a supernova explosion in the past, which could have disturbed the inner binary's orbit and composition. But as discussed before, the abundances observed in the inner binary do not show any peculiarity. In such a case, the tertiary would have been formed elsewhere and was captured dynamically in the current system.

The best fitting age of the binary from the isochrone fitting is 14.5 Myr (Fig.18; left), which is almost twice the median age of a sample of $\beta$ Cep stars observed by *TESS*, which is 7 Myr (Fritzewski et al. 2025). But the age is small compared to the theoretical timescales of the tidal evolution of the system. We use the code JKTABSDIM[12] (based on Zahn 1975, 1977) to calculate theoretical synchronisation and circularisation times. We found that the synchronisation and circularisation timescales are 31 Myrs and 114 Myrs, respectively. This explains the super-synchronous rotation of the components.

### 6.2 Tertiary is a main-sequence star

Case-(ii) SED fitting (centre panel of Fig.17) shows that the tertiary flux is higher than the secondary flux, at all wavelengths. We cannot fit a single isochrone to such a tertiary, and hence, it could not be co-evolving. Instead, we find that such a companion is only possible if it formed later and is metal-rich compared to the inner binary (centre panel of Fig.18). In this case, the tertiary is less massive than the calculated minimum mass. The infrared excess in the SED residuals is also unexplained. Furthermore, in such a case, we would also expect to see the lines of the tertiary in the optical spectra. The above reasons make this case the least favourable of all three cases.

### 6.3 Tertiary is a close binary

Case-(iii) (right panel of Fig.17) is the most probable (and simplistic) case. This case represents a case of a close binary acting as the companion. This gives rise to the expected third light, explains the mass calculated from the RV-PC fitting, and has the same metallicity and age as that of the EB (right panel of Fig.18). The individual contribution of the stars to the total flux is lower than that of the secondary and this would explain why we do not see additional lines in the spectra. Therefore, we conclude that V446 Cep is a co-evolving hierarchical quadruple where all the stars were formed in situ.

## 7 CONCLUSIONS

We analysed the pulsating EB V446 Cep with ten sectors of *TESS* photometry and 72 HERMES spectra. Using detailed light curve modelling and orbital analysis, we found the stellar and orbital parameters of the system. The system contains a 3.808567 d binary with a low mass-ratio of 0.155. We also constrained the atmospheric parameters of the stars from disentangled spectra. The primary was found to be the hotter component with a temperature of 24220 K compared to the 9080 K secondary.

Using the residuals of the binary light curve modelling, we extracted the pulsation frequencies. From the masses and temperatures of the companions, we attribute the pulsations to the primary component. The dominant pulsation frequency is near-harmonic to the orbital frequency. We found no multiplets or significant phase and amplitude variations over the orbital period to suggest that it is a tidally perturbed mode.

We also found significant ETVs for the primary and secondary eclipses. Using pulsation timing of the dominant pulsation frequency, we found a consistent period variation of around 2408 d with an amplitude of 0.15 d. We combined RV and period changes of the dominant pulsation to find that the newly discovered companion has a minimum mass of 4.23 $M_\odot$. We also used astrometric models and *Gaia* astrometric parameters to get orbital parameters of the tertiary orbit.

We explored the formation and evolution of the system with SED modelling and isochrone fitting. We found three feasible cases, out

[12] https://www.astro.keele.ac.uk/jkt/codes/jktabsdim.html

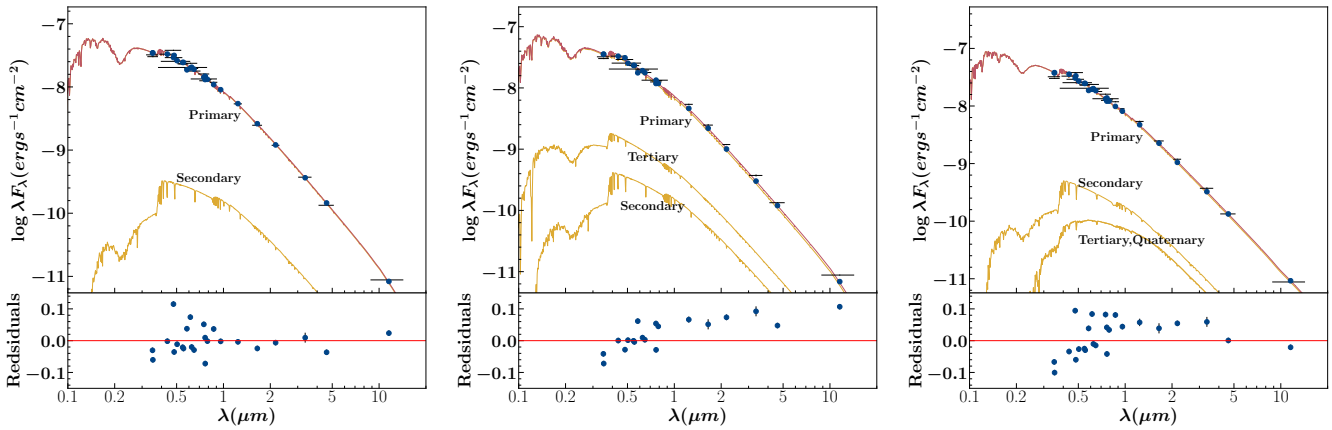


**Figure 17.** Best-fitting Kurucz SED for the binary+compact object case (left), main sequence triple case (centre), and the quadruple case where the third and fourth star have the same SED (right). The yellow lines show the component SEDs, while the red line shows the combination SED. The primary has the maximum flux contribution so its SED is close to the total SED. The dots represent the modelled fluxes and the crosses represent observed fluxes. The bottom panels show residuals for different photometric observations. The errors on the photometry are underestimated as they do not account for eclipses and pulsations, which significantly affect the total observed flux of the system.

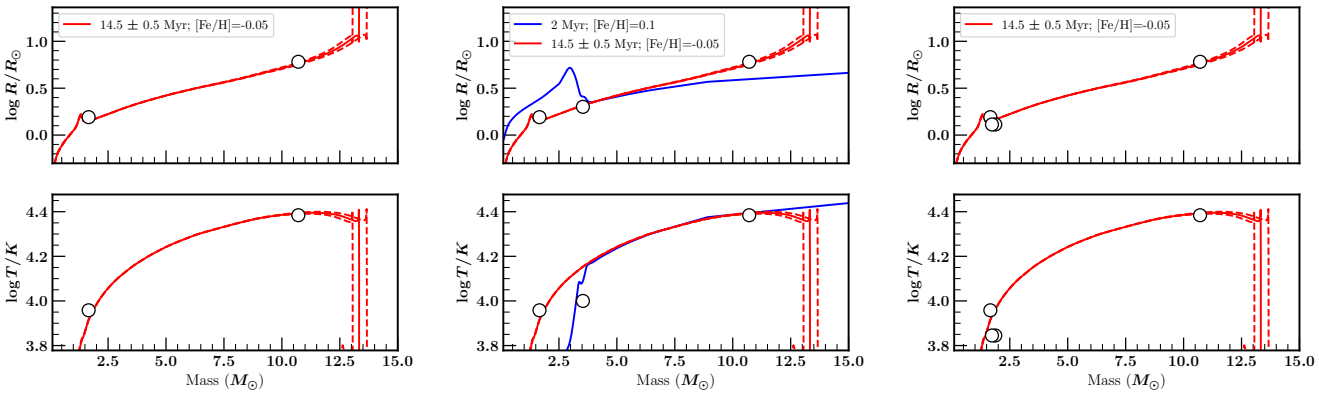


**Figure 18.** Best-fitting MIST isochrones for the binary+compact object case (left), main sequence triple case (centre), and the quadruple case (right). The red isochrone shows the best fit for the pulsating binary system, while the blue line shows an isochrone of 2 Myr. The stars are represented as hollow circles. Their error bars are smaller than their markers.

**Table 8.** Parameters obtained from SED fitting for the three cases discussed in section 6.

| Parameters | Binary (tertiary is compact object) | Triple | Quadruple |
|---|---|---|---|
| $A_v$ | 1.00 | 0.85 | 0.83 |
| $d$ [pc] | 731.6 | 800.0 | 750.0 |
| R [$R_\odot$] | [5.9 1.5] | [5.9, 1.5, 2. ] | [5.9, 1.5, 1.3, 1.3 ] |
| log $g$ | [3.9, 4.3] | [3.9, 4.3, 4.4 ] | [3.9, 4.3, 4.5, 4.5] |
| $T_{\rm eff}$ [K] | [24230, 9080] | [24230, 9500, 10000] | [24220, 9480, 7000, 7000] |
| [Fe/H] | -0.05 | 0.05 | -0.05 |
| Total companion mass [$M_\odot$] | - | 3.5 | 4.4 |
| $\chi^2$ | 23 | 31.0 | 38.0 |

of which we conclude that the most probable case makes V446 Cep a co-evolving 14.5 Myr quadruple system. The configuration of the quadruple was found to be a 2+2 hierarchy where the EB is orbited by a close binary on an orbit of around 2408 d period.

This configuration of multiplicity is the best estimate we could make from the current set of photometric, spectroscopic, and astrometric observations. Nonetheless, it is an estimate, and the exact configuration could be revealed with more observations. However, the stars in the EB are useful and the primary $\beta$ Cep has a good set of observables for detailed evolutionary modelling, especially since we see tentative evidence of tides impacting the pulsations. Thus, tides in such systems are also important to consider in evolution calculations.

## ACKNOWLEDGEMENTS

A. Moharana thanks Jeppe Sinbaek Thomsen for comprehensive discussions on pulsations and light curve modelling. A. Moharana also thanks Dr. Kareem El-Badry for suggesting the checks with GAIAMOCK. The authors also thank Dr. Pierre Maxted and Dr. Barry Smalley for useful discussions.

A. Moharana and JS acknowledge support from the Science and Technology Facilities Council (STFC) under grant number ST/Y002563/1.

A. Miszuda acknowledges the support by the Polish National Science Centre (NCN), grant number 2021/43/B/ST9/02972.

RSR acknowledges support from the French Agence Nationale de la Recherche (ANR) under grant ANR-23-CE31-0009-01 (UnlockPFactor), and from the National Science Center, Poland, through the Sonata BIS 2018/30/E/ST9/00598 and the OPUS grant 2024/53/B/ST9/02630.

KGH acknowledges the support by the NCN through the grant 2023/49/B/ST9/01671.

DMB gratefully acknowledges UK Research and Innovation (UKRI) in the form of a Frontier Research grant under the UK government's ERC Horizon Europe funding guarantee (SYMPHONY; PI Bowman; grant number: EP/Y031059/1), and a Royal Society University Research Fellowship (PI Bowman; grant number: URF\R1\231631).

This work used the greenHPC facility at Keele University, which is supported by the Wolfson Foundation's Funding for places grant.

Based on observations made with the Mercator Telescope, operated on the island of La Palma by the Flemish Community, at the Spanish Observatorio del Roque de los Muchachos of the Instituto de Astrofísica de Canarias. Based on observations obtained with the HERMES spectrograph, which is supported by the Research Foundation - Flanders (FWO), Belgium, the Research Council of KU Leuven, Belgium, the Fonds National de la Recherche Scientifique (F.R.S.-FNRS), Belgium, the Royal Observatory of Belgium, the Observatoire de Genève, Switzerland and the Thüringer Landessternwarte Tautenburg, Germany.

This paper includes data collected with the *TESS* mission, obtained from the Mikulski Archive for Space Telescopes (MAST) at the Space Telescope Science Institute (STScI). Funding for the *TESS* mission is provided by the NASA Explorer Program. STScI is operated by the Association of Universities for Research in Astronomy, Inc., under NASA contract NAS 5–26555. This work has made use of data from the European Space Agency (ESA) mission *Gaia* (https://www.cosmos.esa.int/gaia), processed by the *Gaia* Data Processing and Analysis Consortium (DPAC, https://www.cosmos.esa.int/web/gaia/dpac/consortium). Funding for the DPAC has been provided by national institutions, in particular the institutions participating in the *Gaia* Multilateral Agreement. This work made use of TOPCAT and the STILTS package (Taylor 2005, 2006). This research has made use of the SIMBAD database (Wenger et al. 2000), operated at CDS, Strasbourg, France. This research has made use of the Astrophysics Data System, funded by NASA under Cooperative Agreement 80NSSC25M7105.

## DATA AVAILABILITY

The *TESS* data used in this article are available in the MAST data archive (https://mast.stsci.edu/portal/Mashup/Clients/Mast/Portal.html). The HERMES spectra used in the article are available at: https://doi.org/10.5281/zenodo.17513474. The ETV measurements are available in the online supplementary material corresponding to the article.

## REFERENCES

Aerts C., 2021, Reviews of Modern Physics, 93, 015001
Aerts C., Christensen-Dalsgaard J., Kurtz D. W., 2010, Asteroseismology. Springer Dordrecht, doi:10.1007/978-1-4020-5803-5
Aller A., Lillo-Box J., Jones D., Miranda L. F., Barceló Forteza S., 2020, A&A, 635, A128
Aschenbrenner P., Przybilla N., Butler K., 2023, A&A, 671, A36
Baglin A., et al., 2006, in 36th COSPAR Scientific Assembly. p. 3749
Baran A. S., Koen C., 2021, Acta Astron., 71, 113
Bedding T. R., et al., 2011, Nature, 471, 608
Borkovits T., Rappaport S. A., Hajdu T., Maxted P. F. L., Pál A., Forgács-Dajka E., Klagyivik P., Mitnyan T., 2020, MNRAS, 493, 5005
Borkovits T., Rappaport S. A., Toonen S., Moe M., Mitnyan T., Csányi I., 2022, MNRAS, 515, 3773
Borucki W. J., et al., 2010, Science, 327, 977
Bowman D. M., 2020, Frontiers in Astronomy and Space Sciences, 7, 70
Bowman D. M., 2023, Ap&SS, 368, 107
Bowman D. M., Kurtz D. W., Breger M., Murphy S. J., Holdsworth D. L., 2016, MNRAS, 460, 1970
Bowman D. M., Johnston C., Tkachenko A., Mkrtichian D. E., Gunsriwiwat K., Aerts C., 2019, ApJ, 883, L26
Bowman D. M., Hermans J., Daszyńska-Daszkiewicz J., Holdsworth D. L., Tkachenko A., Murphy S. J., Smalley B., Kurtz D. W., 2021, MNRAS, 504, 4039
Brandt T. D., 2021, ApJS, 254, 42
Briquet M., 2003, PhD thesis, University of Liege, Belgium
Briquet M., Aerts C., Mathias P., Scuflaire R., Noels A., 2003, A&A, 401, 281
Briquet M., Lefever K., Uytterhoeven K., Aerts C., 2005, MNRAS, 362, 619
Briquet M., et al., 2012, MNRAS, 427, 483
Burssens S., et al., 2020, A&A, 639, A81
Burssens S., et al., 2023, Nature Astronomy, 7, 913
Butler K., 1984, PhD thesis, University College London, UK
Castelli F., Kurucz R. L., 2003, in Piskunov N., Weiss W. W., Gray D. F., eds, IAU Symposium Vol. 210, Modelling of Stellar Atmospheres. p. A20 (arXiv:astro-ph/0405087), doi:10.48550/arXiv.astro-ph/0405087
Chaplin W. J., Miglio A., 2013, ARA&A, 51, 353
Charbonneau P., 1995, ApJS, 101, 309
Choi J., Dotter A., Conroy C., Cantiello M., Paxton B., Johnson B. D., 2016, ApJ, 823, 102
Conroy K. E., et al., 2020, ApJS, 250, 34
De Ridder J., Dupret M. A., Neuforge C., Aerts C., 2002, A&A, 385, 572
Dotter A., 2016, ApJS, 222, 8
Duchêne G., Kraus A., 2013, ARA&A, 51, 269
Dziembowski W. A., Pamiatnykh A. A., 1993, MNRAS, 262, 204
El-Badry K., Lam C., Holl B., Halbwachs J.-L., Rix H.-W., Mazeh T., Shahaf S., 2024, The Open Journal of Astrophysics, 7, 100
Eze C. I., Handler G., 2024, ApJS, 272, 25

Foreman-Mackey D., Hogg D. W., Lang D., Goodman J., 2013, PASP, 125, 306
Fritzewski D. J., Vanrespaille M., Aerts C., Guo Z., Hey D., De Ridder J., 2025, A&A, 698, A253
Fuller J., 2021, MNRAS, 501, 483
Fuller J., Kurtz D. W., Handler G., Rappaport S., 2020, MNRAS, 498, 5730
Gaia Collaboration et al., 2016, A&A, 595, A1
Giddings J. R., 1980, PhD thesis, University College London, UK
Grudić M. Y., Hopkins P. F., 2019, MNRAS, 488, 2970
Guo Z., 2021, Frontiers in Astronomy and Space Sciences, 8, 67
Hadrava P., 1995, A&AS, 114, 393
Hajdu G., et al., 2021, ApJ, 915, 50
Handler G., Jayaraman R., Kurtz D. W., Fuller J., Rappaport S. A., 2022, in Szuszkiewicz E., et al., eds, Vol. 12, XL Polish Astronomical Society Meeting. pp 183–186 (arXiv:2201.01722), doi:10.48550/arXiv.2201.01722
Higgins E. R., Vink J. S., Hirschi R., Laird A. M., Sabhahit G. N., 2023, MNRAS, 526, 534
Hippke M., David T. J., Mulders G. D., Heller R., 2019, AJ, 158, 143
Hirschi R., et al., 2025, MNRAS,
Horvat M., Conroy K. E., Pablo H., Hambleton K. M., Kochoska A., Giammarco J., Prša A., 2018, ApJS, 237, 26
Howell S. B., et al., 2014, PASP, 126, 398
Huber D., et al., 2011, ApJ, 743, 143
Ilijic S., Hensberge H., Pavlovski K., Freyhammer L. M., 2004, in Hilditch R. W., Hensberge H., Pavlovski K., eds, Astronomical Society of the Pacific Conference Series Vol. 318, Spectroscopically and Spatially Resolving the Components of the Close Binary Stars. pp 111–113
Irwin J. B., 1952, ApJ, 116, 211
Irwin J. B., 1959, AJ, 64, 149
Jayaraman R., Handler G., Rappaport S. A., Fuller J., Kurtz D. W., Charpinet S., Ricker G. R., 2022, ApJ, 928, L14
Jayaraman R., et al., 2024, ApJ, 975, 121
Jenkins J. M., et al., 2016, in Chiozzi G., Guzman J. C., eds, Society of Photo-Optical Instrumentation Engineers (SPIE) Conference Series Vol. 9913, Software and Cyberinfrastructure for Astronomy IV. p. 99133E, doi:10.1117/12.2233418
Jennings Z., Southworth J., Pavlovski K., Van Reeth T., 2024, MNRAS, 527, 4052
Johnston C., 2021, A&A, 655, A29
Johnston C., Tkachenko A., Van Reeth T., Bowman D. M., Pavlovski K., Sana H., Sekaran S., 2023, A&A, 670, A167
Jones D., et al., 2020, ApJS, 247, 63
Kallinger T., Reegen P., Weiss W. W., 2008, A&A, 481, 571
Kazarovets E. V., Samus N. N., Durlevich O. V., Frolov M. S., Antipin S. V., Kireeva N. N., Pastukhova E. N., 1999, Information Bulletin on Variable Stars, 4659, 1
Kervella P., Arenou F., Mignard F., Thévenin F., 2019, A&A, 623, A72
Keszthelyi Z., Meynet G., Georgy C., Wade G. A., Petit V., David-Uraz A., 2019, MNRAS, 485, 5843
Keszthelyi Z., Puls J., Chiaki G., Nagakura H., ud-Doula A., Takiwaki T., Tominaga N., 2024, MNRAS, 533, 3457
Kolbas V., et al., 2015, MNRAS, 451, 4150
Konacki M., Muterspaugh M. W., Kulkarni S. R., Hełminiak K. G., 2010, ApJ, 719, 1293
Kopal Z., 1959, Close binary systems. Wiley, New York
Kurtz D. W., 2022, ARA&A, 60, 31
Kurtz D. W., et al., 2020, MNRAS, 494, 5118
Kurucz R. L., 1979, ApJS, 40, 1
Langer N., 2012, ARA&A, 50, 107
Lehmann H., Southworth J., Tkachenko A., Pavlovski K., 2013, A&A, 557, A79
Lenz P., Breger M., 2005, Communications in Asteroseismology, 146, 53
Lightkurve Collaboration et al., 2018, Lightkurve: Kepler and TESS time series analysis in Python, Astrophysics Source Code Library (ascl:1812.013)
Maeder A., 1981, A&A, 101, 385
Maeder A., Meynet G., 2000, A&A, 361, 159
Marcadon F., Prša A., 2024, ApJ, 976, 242
Marchant P., Bodensteiner J., 2024, ARA&A, 62, 21
Mayer P., Harmanec P., Pavlovski K., 2013, A&A, 550, A2
Miglio A., et al., 2012, MNRAS, 419, 2077
Mikulášek Z., 2015, A&A, 584, A8
Miszuda A., Guo Z., Townsend R. H. D., 2025, A&A, 702, A203
Moharana A., Hełminiak K. G., Marcadon F., Pawar T., Konacki M., Ukita N., Kambe E., Maehara H., 2023, MNRAS, 521, 1908
Moharana A., et al., 2024, A&A, 690, A153
Mosteller F., Tukey J. W., 1977, Data analysis and regression. A second course in statistics. Pearson
Murphy S. J., Shibahashi H., Kurtz D. W., 2013, MNRAS, 430, 2986
Nelder J. A., Mead R., 1965, The Computer Journal, 7, 308
Nieva M. F., Przybilla N., 2007, A&A, 467, 295
Nieva M. F., Przybilla N., 2012, A&A, 539, A143
Offner S. S. R., Moe M., Kratter K. M., Sadavoy S. I., Jensen E. L. N., Tobin J. J., 2023, in Inutsuka S., Aikawa Y., Muto T., Tomida K., Tamura M., eds, Astronomical Society of the Pacific Conference Series Vol. 534, Protostars and Planets VII. p. 275 (arXiv:2203.10066), doi:10.48550/arXiv.2203.10066
Pavlovski K., Southworth J., Tamajo E., 2018, MNRAS, 481, 3129
Pavlovski K., et al., 2022, A&A, 658, A92
Pavlovski K., Southworth J., Tkachenko A., Van Reeth T., Tamajo E., 2023, A&A, 671, A139
Pierce M. J., Jurcevic J. S., Crabtree D., 2000, MNRAS, 313, 271
Pilecki B., Pietrzyński G., Anderson R. I., Gieren W., Taormina M., Narloch W., Evans N. R., Storm J., 2021, ApJ, 910, 118
Podsiadlowski P., 2010, New Astron. Rev., 54, 39
Prša A., et al., 2016, ApJS, 227, 29
Rappaport S. A., et al., 2021, MNRAS, 503, 254
Rappaport S. A., et al., 2024, A&A, 686, A27
Raskin G., et al., 2011, A&A, 526, A69
Rathour R. S., Hajdu G., Smolec R., Karczmarek P., Hocdé V., Ziółkowska O., Soszyński I., Udalski A., 2024, A&A, 686, A268
Rathour R. S., Smolec R., Hajdu G., Ziółkowska O., Hocdé V., Soszyński I., Udalski A., Karczmarek P., 2025, A&A, 695, A114
Ricker G. R., et al., 2015, Journal of Astronomical Telescopes, Instruments, and Systems, 1, 014003
Rodríguez-Segovia N., et al., 2022, MNRAS, 509, 2885
Rucinski S. M., 1992, AJ, 104, 1968
Rucinski S., 1999, in Hearnshaw J. B., Scarfe C. D., eds, Astronomical Society of the Pacific Conference Series Vol. 185, IAU Colloq. 170: Precise Stellar Radial Velocities. p. 82 (arXiv:astro-ph/9807327), doi:10.48550/arXiv.astro-ph/9807327
Sana H., et al., 2013, in Pugliese G., de Koter A., Wijburg M., eds, Astronomical Society of the Pacific Conference Series Vol. 470, 370 Years of Astronomy in Utrecht. p. 141 (arXiv:1211.4740), doi:10.48550/arXiv.1211.4740
Schootemeijer A., Langer N., Grin N. J., Wang C., 2019, A&A, 625, A132
Simon K. P., Sturm E., 1994, A&A, 281, 286
Southworth J., 2013, A&A, 557, A119
Southworth J., 2015, in Rucinski S. M., Torres G., Zejda M., eds, Astronomical Society of the Pacific Conference Series Vol. 496, Living Together: Planets, Host Stars and Binaries. p. 164 (arXiv:1411.1219), doi:10.48550/arXiv.1411.1219
Southworth J., 2020, The Observatory, 140, 247
Southworth J., Bowman D. M., 2022, Monthly Notices of the Royal Astronomical Society, 513, 3191
Southworth J., Bowman D., 2025, arXiv e-prints, p. arXiv:2509.08426
Southworth J., Bowman D. M., Tkachenko A., Pavlovski K., 2020, MNRAS, 497, L19
Southworth J., Bowman D. M., Pavlovski K., 2021, MNRAS, 501, L65
Steindl T., Zwintz K., Bowman D. M., 2021, A&A, 645, A119
Taylor M. B., 2005, in Shopbell P., Britton M., Ebert R., eds, Astronomical Society of the Pacific Conference Series Vol. 347, Astronomical Data Analysis Software and Systems XIV. p. 29
Taylor M. B., 2006, in Gabriel C., Arviset C., Ponz D., Enrique S., eds, Astro-

nomical Society of the Pacific Conference Series Vol. 351, Astronomical Data Analysis Software and Systems XV. p. 666
Telting J. H., Schrijvers C., 1997, A&A, 317, 723
Tempesti P., 1971, Information Bulletin on Variable Stars, 596, 1
Themeßl N., et al., 2018, MNRAS, 478, 4669
Tkachenko A., et al., 2012, MNRAS, 424, L21
Tkachenko A., et al., 2014, MNRAS, 438, 3093
Tkachenko A., et al., 2016, MNRAS, 458, 1964
Tkachenko A., Pavlovski K., Serebriakova N., Bowman D. M., IJspeert L., Gebruers S., Southworth J., 2024, A&A, 683, A252
Torres G., Andersen J., Giménez A., 2010, A&ARv, 18, 67
Torres G., Sandberg Lacy C. H., Pavlovski K., Feiden G. A., Sabby J. A., Bruntt H., Viggo Clausen J., 2014, ApJ, 797, 31
Van Reeth T., Southworth J., Van Beeck J., Bowman D. M., 2022, A&A, 659, A177
Van Reeth T., Johnston C., Southworth J., Fuller J., Bowman D. M., Poniatowski L., Van Beeck J., 2023, A&A, 671, A121
Wagg T., Johnston C., Bellinger E. P., Renzo M., Townsend R., de Mink S. E., 2024, A&A, 687, A222
Walker G., et al., 2003, PASP, 115, 1023
Weiss W. W., et al., 2014, PASP, 126, 573
Weiss W. W., et al., 2021, Universe, 7, 199
Wenger M., et al., 2000, A&AS, 143, 9
Wolf M., Zejda M., de Villiers S. N., 2008, MNRAS, 388, 1836
Wu R.-Q., Zhu C.-H., Lü G.-L., Wang Z.-J., Liu H.-L., 2021, Research in Astronomy and Astrophysics, 21, 129
Zahn J. P., 1975, A&A, 41, 329
Zahn J. P., 1977, A&A, 57, 383
Zasche P., Wolf M., 2007, Astronomische Nachrichten, 328, 928
Zhang V., Rappaport S., Jayaraman R., Kurtz D. W., Handler G., Fuller J., Borkovits T., 2024, MNRAS, 528, 3378
Zucker S., Mazeh T., 1994, ApJ, 420, 806
de Mink S. E., Sana H., Langer N., Izzard R. G., Schneider F. R. N., 2014, ApJ, 782, 7

## APPENDIX A: DIAGNOSTICS OF PHOEBE2 MODELLING

The corner plot for the adopted MCMC chain is shown in Fig.A1 The final residuals after the Nelder-Mean optimisation for different sectors are given in Fig.A2. The MCMC residuals are shown in black for comparision.

## APPENDIX B: BROADENING FUNCTIONS

The broadening function (BF; Rucinski 1992) has the capability to visualise intrinsic stellar effects like rotational broadening, spots, and pulsations (Moharana et al. 2023). To spot similar variations in the $\beta$ Cep component of V446 Cep, we calculated BF using the HERMES spectra. The BF was calculated using the algorithm described in Rucinski (1999). We modified a single-order BF code, BF-RVPLOTTER[13], to calculate multi-order BFs. The BF was calculated in a wavelength range of 4000-5000 Å, 5000-6000 Å, and 6000-7000 Å. As our template, We used a synthetic spectrum generated with the code SPECTRUM using model atmospheres from ATLAS9, abundances from, and line lists from . The template created had a temperature of 18800 K, log $g$ of 3.5 dex, [M/H] of 0.5 dex with projected rotational velocity ($v\sin i$) of 1 km s$^{-1}$. The final BFs generated were smoothed with a Gaussian smoother of a 10 km s$^{-1}$ rolling window. We find that the BFs show wavelength-dependent variability. In Fig.B1, we show the BF variations observed in the spectra from secondary (Fig.B1; top panels) and primary (Fig.B1; bottom panels) eclipses. PP and OP in the plots denote pulsation phase and orbital phase, respectively. The time reference for the phase calculation is the same.

[13] https://github.com/mrawls/BF-rvplotter

**Table E1.** Times of minima of the primary and secondary eclipses from the *TESS* light curve of V446 Cep. The full table is available in machine-readable format in the online supplementary material.

| Time BJD−2457000 | Cycle no. | 1$\sigma$ error (d) |
|---|---|---|
| 1740.34139 | 0.0 | 0.00018 |
| 1742.26266 | 0.5 | 0.00042 |
| 1744.15017 | 1.0 | 0.00017 |
| 1746.07244 | 1.5 | 0.00049 |
| 1747.95882 | 2.0 | 0.00017 |
| 1751.76608 | 3.0 | 0.00023 |
| 1753.68944 | 3.5 | 0.00039 |
| 1755.57589 | 4.0 | 0.00017 |
| 1757.49808 | 4.5 | 0.00038 |
| 1759.38381 | 5.0 | 0.00017 |

*Notes.* Half-integer cycle numbers refer to secondary eclipses.

## APPENDIX C: FILTERING FREQUENCIES

We calculated power spectral density (PSD) for each set of consecutive sectors available (Fig.C1) using the Lomb-Scargle periodogram. We visually inspected all the extracted frequencies that are higher than the $f_{\rm orb}$ and then rejected them if either: (i) they were not significant in all the light curve sets (Fig.C1; top left), or (ii) they had S/N < 5 and were exact harmonics of $f_{\rm orb}$ (Fig.C1; top middle), or (iii) they had extremely different PSD profiles in different sets (Fig.C1; top right). We also rejected multiple frequencies detected in the DFT that were lower in amplitude than the central frequency but inside the central lobe of the window function of the PSD spectrum, and hence unresolved. The accepted frequencies are shown in the bottom panel of Fig.C1.

## APPENDIX D: ASTROMETRY SIMULATIONS OF SYSTEMS WITH KNOWN 3D GEOMETRY

We compiled a list of compact hierarchical triples (CHT), which have precisely measured parameters that define a system's 3D geometry. From Borkovits et al. (2020, 2022); Moharana et al. (2023, 2024), and Rappaport et al. (2024), we get all orbital parameters, including $i_2$ and $\Omega_2$. We then calculated theoretical RUWE using GAIAMOCK and compared the deviation ($\Delta_{\rm RUWE}$) from observed RUWE values. We find that most of the systems have consistent observed and simulated RUWE, within an error of 0.3 (Fig.D1). The systems that have a large discrepancy with the simulations have RUWE greater than 2. This shows that models with $\Delta_{\rm RUWE}$ less than 0.3 are acceptable solutions for V446 Cep.

## APPENDIX E: ECLIPSE TIMINGS

In Table E1, we provide the times of primary and secondary minima of V446 Cep derived from the *TESS* light curve using the procedure described in Section 5.1.

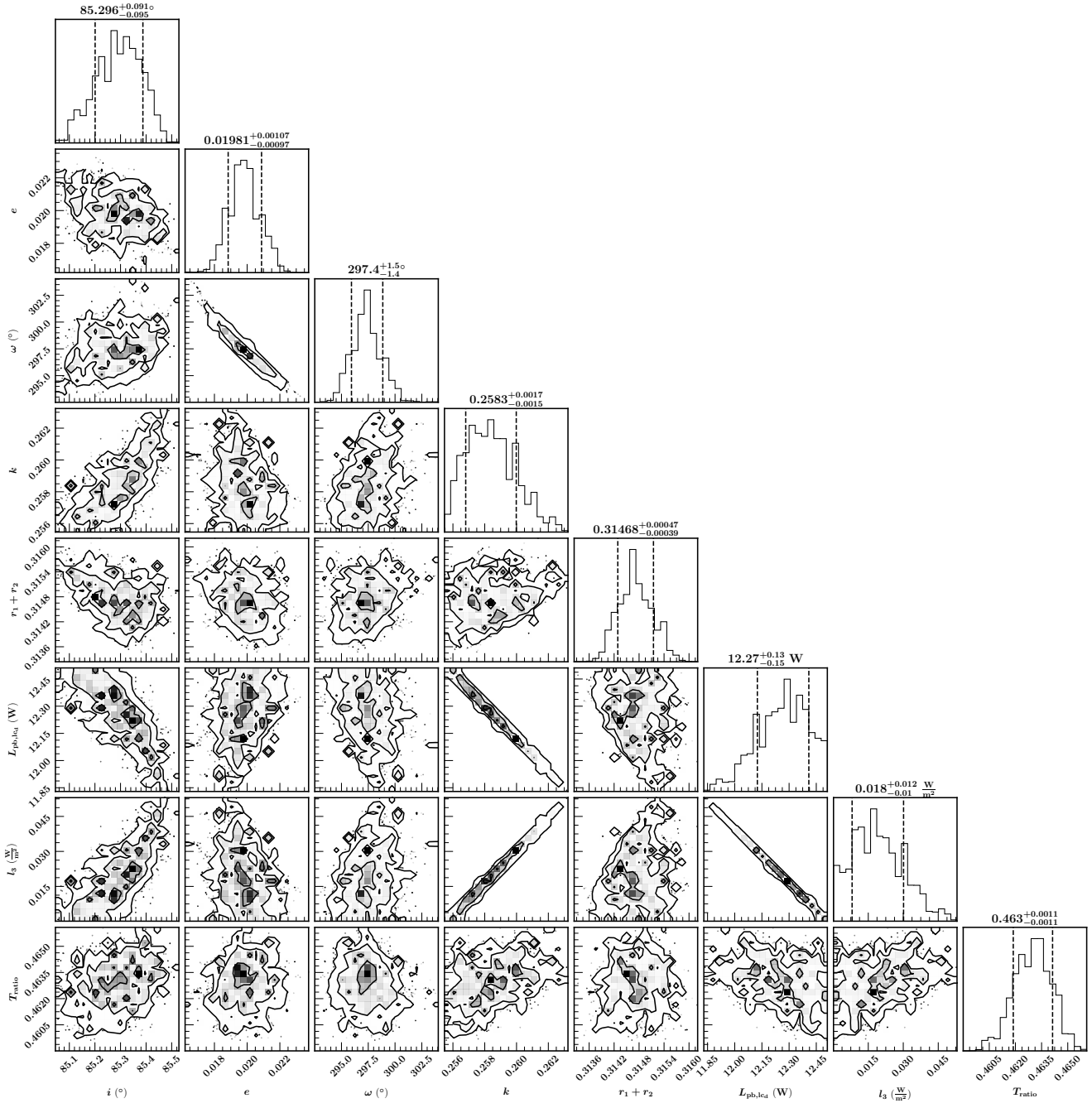


**Figure A1.** Corner plots for the PHOEBE2 MCMC sampling of stellar and orbital parameters of the EB in V446 Cep.

This paper has been typeset from a TEX/LATEX file prepared by the author.

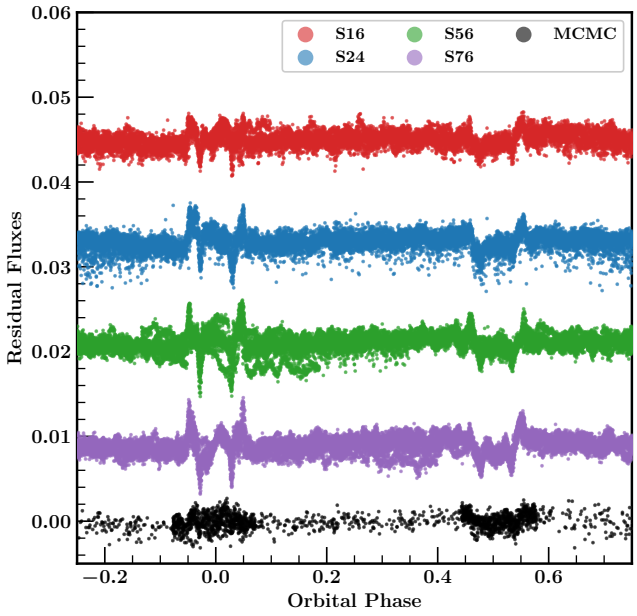


**Figure A2.** Light curve residuals after subtraction of PHOEBE2 models.

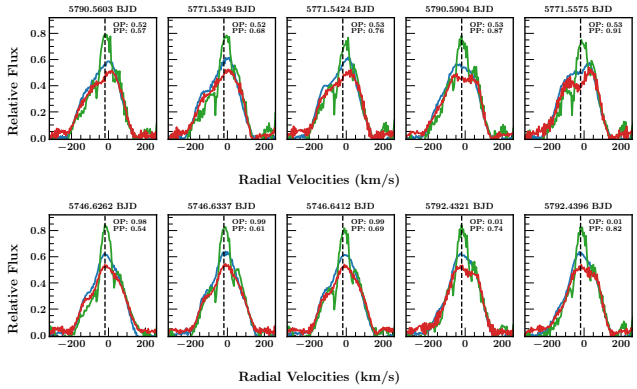


**Figure B1.** BF variation during secondary (total) eclipse (top) and primary eclipse (bottom). BF in blue, green, and red are extracted from spectra in regions of 4000-5000 A°, 5000-6000 A°, and 6000-7000 A°, respectively. The dashed black line is the gamma velocity.

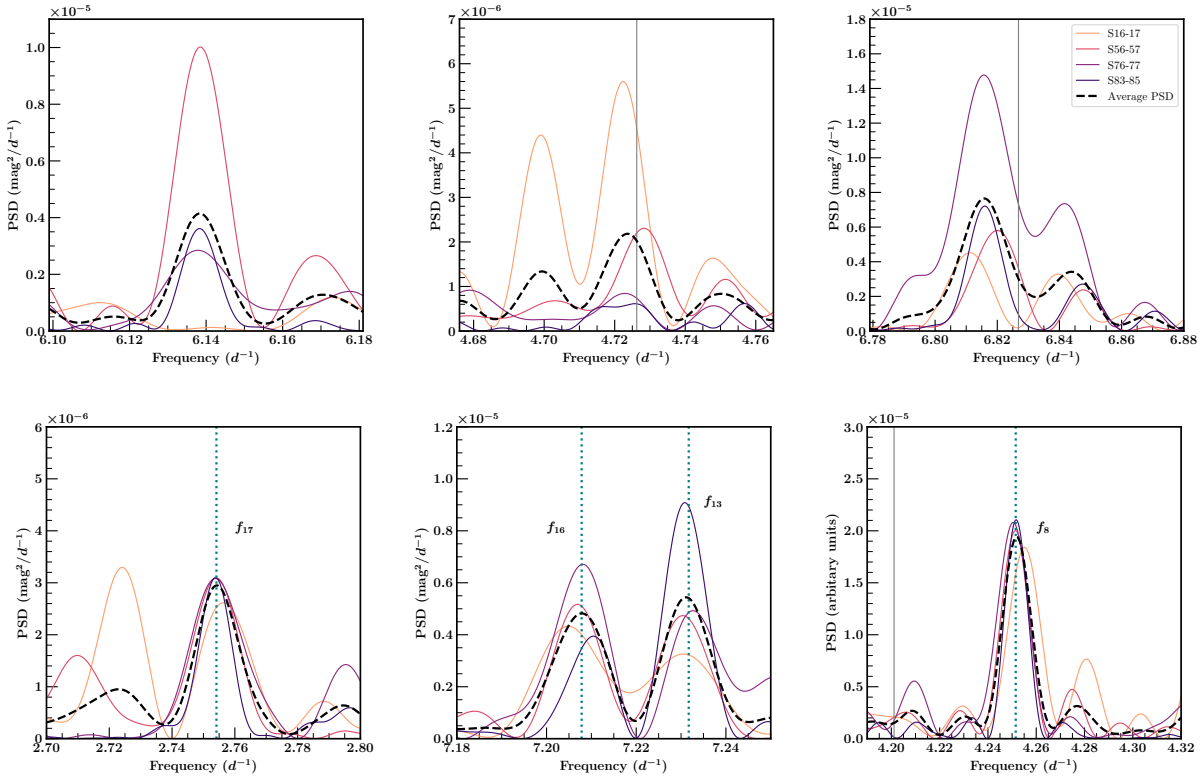


**Figure C1.** PSD profiles for different sectoral sets and pulsations. The top panel shows the different frequencies that were found in the initial DFT search but rejected due to our stability criteria. The lower panel shows the accepted frequencies. The grey vertical lines represent the orbital harmonics and the teal dashed lines represent the position of the accepted frequencies.

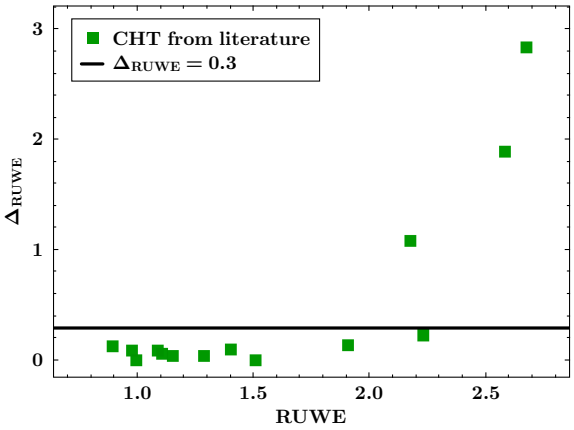


**Figure D1.** Comparison of $\Delta_{\mathrm{RUWE}}$ for different compact hierarchical triples with measurements of all orbital parameters. $\Delta_{\mathrm{RUWE}}$ is calculated by taking the absolute difference of RUWE calculated using a GAIAMOCK model and the actual RUWE value observed with GAIA.